

1  
2  
3 **1 Using UAS optical imagery and SfM photogrammetry to characterize the surface grain size of**  
4 **2 gravel bars in a braided river (Vénéon River, French Alps)**

5  
6  
7 3 Daniel Vázquez-Tarrió\* <sup>1,2,3</sup>, Laurent Borgniet<sup>1</sup>, Frédéric Liébault<sup>1</sup> and Alain Recking<sup>1</sup>

8  
9 4 \*Corresponding author. Tel.: (+33) 442971500. [vazqueztarrio@cerege.fr](mailto:vazqueztarrio@cerege.fr)

10  
11 5 <sup>1</sup>Université Grenoble Alpes, Irstea, UR ETNA, 2 rue de la Papeterie-BP 76, F-38402 St-Martin-d'Hères,  
12  
13 6 France

14  
15 7 <sup>2</sup>Fundación para el Fomento en Asturias de la Investigación Científica Aplicada y la Tecnología  
16  
17 8 (FICYT), c/ Cabo Noval, nº11, 1º C, 33007 Oviedo, Spain

18  
19 9 <sup>3</sup>Centre européen de recherche et d'enseignement de géosciences et de l'environnement (CEREGE),  
20  
21 10 CNRS UMR 7330, Europôle de l'Arbois, BP 80, 13545 Aix-en-Provence, France  
22  
23  
24  
25  
26  
27  
28  
29  
30  
31  
32  
33  
34  
35  
36  
37  
38  
39  
40  
41  
42  
43  
44  
45  
46  
47  
48  
49  
50  
51  
52  
53  
54  
55  
56  
57  
58  
59

60  
61  
62  
63  
64  
65  
66  
67  
68  
69  
70  
71  
72  
73  
74  
75  
76  
77  
78  
79  
80  
81  
82  
83  
84  
85  
86  
87  
88  
89  
90  
91  
92  
93  
94  
95  
96  
97  
98  
99  
100  
101  
102  
103  
104  
105  
106  
107  
108  
109  
110  
111  
112  
113  
114  
115  
116  
117  
118

11 **Abstract**

12 This paper explores the potential of unmanned aerial system (UAS) optical aerial imagery to characterize  
13 grain roughness and size distribution in a braided, gravel-bed river (Vénéon River, French Alps). With  
14 this aim in view, a Wolman field campaign (19 samples) and five UAS surveys were conducted over  
15 the Vénéon braided channel during summer 2015. The UAS consisted of a small quadcopter carrying a  
16 GoPro camera. Structure-from-Motion (SfM) photogrammetry was used to extract dense and accurate  
17 three-dimensional point clouds. Roughness descriptors (roughness heights, standard deviation of  
18 elevation) were computed from the SfM point clouds and were correlated with the median grain size of  
19 the Wolman samples. A strong relationship was found between UAS-SfM-derived grain roughness and  
20 Wolman grain size. The procedure employed has potential for the rapid and continuous characterization  
21 of grain size distribution in exposed bars of gravel-bed rivers. The workflow described in this paper has  
22 been successfully used to produce spatially continuous grain size information on exposed gravel bars  
23 and to explore textural changes following flow events.

24 *Keywords:* SfM, photogrammetry, grain size, roughness, braided rivers, gravel bed rivers

## 1. Introduction

Grain roughness and grain size distribution (GSD) of riverbed sediment in gravel-bed rivers have been a long-standing focus of interest for fluvial scientists (Rice and Church, 1998, 2010). On the one hand, grain roughness influences flow resistance, the variability and magnitude of shear stress (Naot, 1984; Robert et al., 1992) and the sediment supply of bedload transport (Paola and Seal, 1995; Vericat et al., 2008), and it is an important parameter in hydraulic modelling (Milan and Heritage, 2012). On the other hand, GSD exerts a significant control on the habitat of many benthic organisms.

In gravel-bed streams, grain size and surface roughness shows substantial heterogeneity at different scales (Leopold et al., 1964; Bluck, 1976; Lisle and Madej, 1992; Ashworth, 1996; Rice and Church, 2010; Milan, 2013; Storz-Peretz and Laronne, 2013; Guerit et al., 2014). At the reach scale, it may be represented by patches or facies of similar texture and grain size (Dietrich et al., 2005; Nelson et al., 2009), defining a textural mosaic. This sedimentary mosaic is particularly complex in braided settings, where the spatial distribution of patches reflects the main morphological components of the braided landform (Storz-Peretz and Laronne, 2013; Guerit et al., 2014).

Development of a completely satisfactory method for measuring grain size and surface roughness in gravel-bed rivers (Hodge et al., 2009a) has been made difficult by the multiscale heterogeneity of riverbed sediment. The most widely followed procedure by fluvial scientists has been the grid-by-number Wolman count (Wolman, 1954; Rice and Church, 1996; Bunte and Abt, 2001). Surface grain size has also been measured using the photosieving approach, which uses high-resolution close-range imagery (taken 1–2 m above ground level) and image processing techniques (Ibekken and Schleyer, 1986; Butler et al., 2001; Rubin, 2004; Graham et al., 2005; Buscombe, 2008; Detert and Weibrecht, 2013). However, while these methods provide rapid and objective ways for sampling grain size, they are best suited for patch-scale studies (Heritage and Milan, 2009; Milan and Heritage, 2012; Woodget, 2015). This is because a large number of samples is needed for a complete characterization of the large-scale sedimentary mosaic (Woodget, 2015). Consequently, fluvial scientists and engineers require a more rapid and objective technique that is capable of providing fast, continuous, and accurate grain size measurements at river reach scales (a few hundred meters in length).

178  
179  
180 52 Remote sensing approaches have revolutionized the production of fluvial topographic data over the last  
181  
182 53 two decades (Hohenthal et al., 2011; Brasington et al., 2012), and these new technologies could deliver  
183  
184 54 a satisfying alternative to the classical ways of measuring grain size and surface roughness (Heritage  
185  
186 55 and Milan, 2009; Brasington et al., 2012; Woodget, 2015). Carbonneau et al. (2004, 2005), Verdu et al.  
187  
188 56 (2005), Dugdale et al. (2010), and Tamminga et al. (2014) have successfully employed high-resolution  
189  
190 57 aerial imagery and image texture analysis for grain size determination over large areas, the so-called  
191  
192 58 aerial photosieving approach. This method depends on high-resolution images and light conditions as  
193  
194 59 well as sediment color and texture, and they are limited by pixel size and the need for field calibration  
195  
196 60 (Carbonneau et al., 2005; Verdú et al., 2005). Dugdale et al. (2010) used manual calibration performed  
197  
198 61 directly on the aerial images to replace field data. However, a systematic bias was identified in their  
199  
200 62 results, leading to a consistent overestimation of median grain size. Aerial-image calibration is restricted  
201  
202 63 by the user's ability to discriminate smaller size classes and by pixel bleeding effects (lighter colored  
203  
204 64 stones falsely illuminate adjacent pixels, resulting in clasts appearing to be larger than they actually are).  
205  
206 65 Another alternative approach is based on the use of terrestrial laser scanning (TLS). Several recent  
207  
208 66 studies demonstrate that TLS-derived three-dimensional point clouds provide grain-scale altimetric  
209  
210 67 fields that can be used to infer grain size (Smart et al., 2004; Entwistle and Fuller, 2009; Hodge et al.,  
211  
212 68 2009a, b; Hollenthal et al., 2011; Milan and Heritage, 2012). Based on this, Heritage and Milan (2009)  
213  
214 69 and Brasington et al. (2012) used grain roughness obtained from TLS point clouds to retrieve grain size  
215  
216 70 data in gravel-bed rivers. Also, Milan et al. (2009) and Milan and Heritage (2012) showed grain  
217  
218 71 roughness change maps derived from TLS data. However, TLS surveys are expensive and time-  
219  
220 72 consuming for large-scale applications.

221 73 The recent growth and spread of unmanned aerial systems (UASs), coupled with the development and  
222  
223 74 improvement of SfM (Structure from Motion) algorithms (Westoby et al., 2012; Fonstad et al., 2013;  
224  
225 75 Dietrich, 2016; Smith et al., 2016), has enabled the production of highly useful topographic models of  
226  
227 76 fluvial surfaces (Brasington et al., 2012; Micheletti et al., 2014, 2015; Tamminga et al., 2014). The  
228  
229 77 UAS-based SfM photogrammetry provides reconstructions of unvegetated and exposed fluvial  
230  
231 78 topography comparable to those derived by airborne and terrestrial LiDAR (Westoby et al., 2012; Smith  
232  
233 79 and Vericat, 2015), with the main advantage of less expensive equipment. Therefore UAS-based SfM

237  
238  
239 80 photogrammetry could seemingly provide high quality, spatially distributed roughness and morphology  
240  
241 81 data that are needed by hydraulic and morphodynamics models (Tamminga et al., 2014). For example,  
242  
243 82 some recent morphodynamic models (i.e., Lauer et al., 2016) considered lateral variations in grain size,  
244  
245 83 and UAS-derived SfM terrain models may have the potential to feed them with the required data in this  
246  
247 84 regard.

248  
249 85 This paper reports the testing of optical imagery acquired from UAS in connection with SfM and  
250  
251 86 multiview stereo (MVS) photogrammetry to retrieve the GSD of surface bed sediment in a braided  
252  
253 87 gravel-bed river (Vénéon River, French Alps). As it was already mentioned above, previous TLS  
254  
255 88 experiments (Aberle and Smart, 2003; Heritage and Milan, 2009; Brasington et al., 2012) showed that  
256  
257 89 surface roughness computed from 3D point clouds can be used as a proxy of grain size in gravel beds.  
258  
259 90 Here we followed the same approach, using instead SfM-derived point clouds. Three main objectives  
260  
261 91 guided this research: (i) determine the best roughness metric for a percentile estimate from 3D point  
262  
263 92 clouds; (ii) explore whether capturing the spatial variability of surface grain size is possible from  
264  
265 93 distributed roughness information; and (iii) investigate whether detecting changes in surface grain size  
266  
267 94 from roughness information is feasible.

## 268 95 **2. Study site**

269  
270 96 The Vénéon River is a tributary to the Romanche River in the Southern French Alps, draining a 316-  
271  
272 97 km<sup>2</sup> catchment in the Ecrins Massif (Figs. 1A, B). The physical landscape of the basin is dominated by  
273  
274 98 steep rocky slopes, colluvium deposits, and modern and relict periglacial and glacial landforms. Current  
275  
276 99 climate conditions are those typical of a continental, relatively dry and cold climate. The main water  
277  
278 100 source of the Vénéon is La Pilatte glacier, determining a glacial-nival hydrological regime, with the  
279  
280 101 highest discharges between May and August related to snow and glacier melting. High-magnitude flood  
281  
282 102 discharges are related to high temperatures combined with the occurrence of storm-induced heavy  
283  
284 103 rainfalls. The lowest discharges occur between January and March when snowfall dominates. An EDF  
285  
286 104 (Electricité de France) gauging station that has gathered data from 1989 to the present is located  
287  
288 105 upstream of the study site. The mean hourly discharge of this gauging record is 12 m<sup>3</sup> s<sup>-1</sup>, while the  
289  
290 106 maximum and minimum hourly discharges are 206 and 0.1 m<sup>3</sup> s<sup>-1</sup>, respectively. The estimated biannual  
291  
292 107 and decadal peak discharges are 110 and 168 m<sup>3</sup> s<sup>-1</sup>, respectively.

296  
297  
298 108 The study reach comprises a 2.5-km-long and 100- to 200-m-wide river reach where the Vénéon  
299  
300 109 develops a braided planform (Fig. 1C). This braided channel is located upstream of a major obstruction  
301  
302 110 related to a large left-bank rock avalanche deposit. The mean channel slope is 0.013. The catchment  
303  
304 111 area at the study reach is 235 km<sup>2</sup>. Two single dominant channels can generally be distinguished within  
305  
306 112 the overall braided plain. Several seasonal bar-top channels that cut bar surfaces are present. Water flows  
307  
308 113 permanently in the two main anabranches, while bar-top channels are only active during summer high  
309  
310 114 flow events. A 20-m-high hydropower dam (the *Plan du Lac* dam) was built between 1941 and 1943  
311  
312 115 immediately downstream of the study reach (Fig. 1). This hydropower dam is managed by EDF.  
313  
314 116 Bed sediment of the study site is mainly composed of well-rounded and subspherical granitic and  
315  
316 117 metamorphic gravels and cobbles. On exposed gravel bars, the bed sediment is randomly packed,  
317  
318 118 exhibiting a ‘normally loose’ state (*sensu* Church, 1978) without strong imbrication or well-developed  
319  
320 119 grain arrangements (e.g., clusters, stone lines). Discrete small patches (decametric to metric scales) of  
321  
322 120 sand and fine gravel are spread throughout the coarse framework of gravel bars. Conversely, the  
323  
324 121 underwater channel is depleted in sand sediment; and the bed state is ‘underloose’, composed mainly of  
325  
326 122 closely packed and imbricated coarse particles and grain structures.

### 327 123 **3. Material and methods**

#### 328 329 124 *3.1. Field data acquisition*

##### 330 331 125 *3.1.1. UAS surveys*

332  
333 126 Five UAS flights were carried out over the study reach between April and July 2015 using the same  
334  
335 127 unmanned vehicle, a rotatory-wing quadcopter equipped with a GPS for automate flights (Fig. 1C). The  
336  
337 128 capabilities of the vehicle were limited to favorable weather conditions (no rain, wind velocity up to 11  
338  
339 129 m s<sup>-1</sup>). Flight height was ~30 m, and the average flight velocity was ~5 m s<sup>-1</sup>. Images were taken at 1-s  
340  
341 130 intervals using a GoPro HERO 3+ Silver camera (2.77 mm focal length) that was mounted on a platform  
342  
343 131 in the base of the quadcopter. Images were recorded with a resolution of 5 Mpx (2624 × 1968 pixels),  
344  
345 132 using a narrow field of view (28 mm equivalent focal length).

346  
347 133 The SfM-derived point clouds were georeferenced using a set of 92 ground control points (GCPs; Fig.  
348  
349 134 1C) marked along the study reach using a target design automatically detected by the photogrammetric  
350  
351 135 software (AgiSoft PhotoScan). The targets were deployed in the field and this operation took between 1

355  
356  
357 136 and 2 hours before every flight. To save time during the successive drone surveys, target positions were  
358  
359 137 marked with paint in those areas overlapping over consecutive flights. The GCP coordinates were  
360  
361 138 measured in the RGF Lambert 93 coordinate system (EPSG 2154) using a dGPS in RTK (Real Time  
362  
363 139 Kinematic) mode (10 s). A unique position of the dGPS receiver was chosen on an elevated point  
364  
365 140 covering the whole study reach, where good satellite constellation coverage was achieved. Furthermore,  
366  
367 141 to increase the accuracy of dGPS data, the coordinates of the receiver position were referred to those of  
368  
369 142 a permanent geodetic point from the IGN (National Geographic Institute) network during post-  
370  
371 143 processing.

### 372 373 144 *3.1.2. Pebble counts on exposed gravel bars*

374  
375 145 A data set of 19 Wolman pebble counts was collected in the study reach. These samples were taken  
376  
377 146 between March and May 2015 on exposed gravel bars (Fig. 1C). Sample locations were chosen to be  
378  
379 147 representative of the dominant sediment facies. Each pebble count consisted of 100 grains collected  
380  
381 148 along two ~50 m sampling lines spaced ~5 m apart. Sampling of grains was done systematically,  
382  
383 149 extracting them at every 1 m intersection along a tape (around twice the largest grain size visually  
384  
385 150 estimated in the field). To minimize the operator's bias, all the grains were selected and measured by  
386  
387 151 the same person. Metallic templates were used to measure the *b*-axis of grains > 8 mm and to classify  
388  
389 152 them into half- $\Psi$ size classes. Smaller grains were classified into two groups: grains between 4 and 8  
390  
391 153 mm and grains <4 mm. In addition, the coordinates of the central point of each sampling area were  
392  
393 154 measured using a GPS device.

394 155 Average  $D_{50}$  and  $D_{84}$  of exposed gravel bars were 39 and 81 mm, respectively. The average percentage  
395  
396 156 of fine sediment (<8 mm) was 18% ( $\pm 9\%$ ). In addition, GSDs have been truncated at 8 mm, following  
397  
398 157 Rice (1995) who found that particles finer than 8 mm are underrepresented in pebble counts and should  
399  
400 158 consequently not be considered. Average  $D_{50}$  and  $D_{84}$  of truncated GSDs were 46 and 87 mm,  
401  
402 159 respectively (Fig. 2).

### 403 404 160 *3.2. Point cloud processing*

#### 405 406 161 *3.2.1. SfM photogrammetry*

407  
408 162 The UAS images were processed using Agisoft PhotoScan. This software follows the typical steps of  
409  
410 163 SfM-MVS photogrammetry (Remondino et al., 2014). First, it searches for common features across  
411  
412  
413

414  
415  
416 164 overlapping images and finds points that are stable under viewpoint. Afterwards it solves the intrinsic  
417  
418 165 and extrinsic orientation parameters of the camera using a bundle-adjustment algorithm (Robertson and  
419  
420 166 Cipolla, 2009; Semyonov, 2011; Verhoeven et al., 2012; Javernick et al., 2014; Woodget, 2015) and  
421  
422 167 uses the Brown model to correct image distortions related to the camera lens (Brown, 1966; Agisoft,  
423  
424 168 2013; Woodget, 2015). In the third stage, PhotoScan makes a densification of the point cloud using a  
425  
426 169 dense multiview stereo reconstruction.

427  
428 170 As a result of this workflow, a dense point cloud in an arbitrary coordinate system is produced.  
429  
430 171 PhotoScan can transform the derived model into the absolute coordinate system. To accomplish this,  
431  
432 172 GCPs should be manually identified and coordinates imported into the user interface (Javernick et al.,  
433  
434 173 2014). In theory, this process only requires a minimum of three GCPs (James and Robson, 2012, 2014);  
435  
436 174 in practice, more GCPs will produce a better registration of the model. Here we used a large number of  
437  
438 175 GCPs (~90) to achieve a good alignment quality. In addition, an optimization transformation to reduce  
439  
440 176 nonlinear distortions and increase the quality of model registration (Agisoft, 2013; Javernick et al., 2014;  
441  
442 177 Woodget, 2015) was applied. The optimization procedure minimizes geometric distortions by using the  
443  
444 178 known GCP positions to refine the camera lens model and realign the images. Then the geometry of the  
445  
446 179 model is rebuilt after the optimization process.

447  
448 180 Using the Agisoft PhotoScan workflow and its custom algorithms (Fig. 3), we produced five different  
449  
450 181 SfM point clouds, corresponding to each UAS survey (Fig. 1C). Average point densities ranged from  
451  
452 182 40 to 900 points/m<sup>2</sup> (Table 1). We also derived an orthophoto mosaic with a 2-cm pixel resolution for  
453  
454 183 each UAS survey.

455  
456 184 PhotoScan point clouds were finally post-processed using Cloud Compare (Cloud Compare 2.6.2.,  
457  
458 185 2015). In the first step, we filtered and smoothed each UAS-SfM point cloud. Visual assessment revealed  
459  
460 186 some isolated erroneous points. We used the SOR (Statistical Outlier Removal) and noise filters  
461  
462 187 available on Cloud Compare to remove them: the former removes the outliers from the 3D point cloud;  
463  
464 188 the latter works as a low pass filter, locally fitting a plan around each point and removing the points too  
465  
466 189 far away from the fitted plan.

467  
468 190 The planimetric accuracy of 3D point clouds, appraised from the GCPs, is 8–12 cm. To evaluate the  
469  
470 191 altimetric precision, 71 points were measured with a dGPS in RTK mode (10 s) on a gravel bar: the

473  
474  
475 192 standard deviation of Z-differences between the dGPS and the UAS-SfM data ( $\pm 5.3$  cm) was used as a  
476  
477 193 measure of the vertical precision of the point clouds.  
478

479 194 The resolution of the SfM models (position uncertainty of each point in the point clouds) was quantified  
480  
481 195 using the flat surface of a road located on the right bank of the river (Fig., 1C), assuming that on a planar-  
482  
483 196 scanned surface the local difference of the point cloud heights should be 0 (Lague et al., 2013; Smith  
484  
485 197 and Vericat, 2015). For each point belonging to the road, we estimated the average difference of  
486  
487 198 elevation to the mean in a 10-cm moving window. This value was then averaged for all the points located  
488  
489 199 on the road and assumed as a descriptor of point position uncertainty. In this way, we estimated a  
490  
491 200 resolution of  $\pm 0.7$  cm for the point clouds (Table 1).  
492

### 493 201 3.2.2. Roughness metrics

494 202 Different metrics have been used to characterize surface roughness of fluvial sediments. These can be  
495  
496 203 grouped in three different types: (i) roughness height  $rh$  (Gomez, 1993), the difference in height between  
497  
498 204 the top of the bed sediment and the locally averaged topographic surface; (ii) twice the standard  
499  
500 205 deviation ( $2\sigma_z$ ) of elevations in a given area (Heritage and Milan, 2009); and (iii) the root mean square  
501  
502 206 height ( $RMSH$ ), the standard deviation of heights in a given area for which the average slope has been  
503  
504 207 detrended (Aberle and Smart, 2003; Brasington et al., 2012; Storz-Peretz and Laronne, 2013).  
505

506 208 The roughness height was obtained by computing the difference in elevation between each point in the  
507  
508 209 point cloud and the least-squares best-fitting plane computed on its nearest neighbors, within a kernel  
509  
510 210 distance of a specified size. This was achieved using the Cloud Compare roughness tool. To compute  
511  
512 211 the standard deviation of elevations, we first built a regular grid of a given size, and we assigned to each  
513  
514 212 node the standard deviation of elevation for all the points falling within the grid cell. Finally, we  
515  
516 213 estimated the  $RMSH$  following a procedure similar to Brasington et al. (2012) and Rychov et al. (2012).  
517  
518 214 A regular-size grid was built, and the average elevation value for all the points falling in the cell was  
519  
520 215 assigned to each cell node. Then a Delaunay triangulation was used to interpolate a height mesh from  
521  
522 216 this grid. At that point, we subtracted the value of elevation in the mesh from the elevation data of the  
523  
524 217 SfM point cloud. Finally, we took these differences and built a new grid, assigning to each cell node the  
525  
526 218 standard deviation of the residuals falling in the cell.  
527  
528  
529  
530  
531

532  
533  
534 219 Cloud Compare was used to calculate these three different roughness metrics from the SfM point clouds.  
535  
536 220 Once computed, roughness metrics were compared with grain size percentiles to find the best grain size  
537  
538 221 proxy. At the same time, we evaluated different sizes for the kernel radius used for the  $rh$  estimates and  
539  
540 222 the grid size utilized during the  $\sigma_z$  and  $RMSH$  computations. We found an optimum radius of 50 cm (two  
541  
542 223 to three times the largest clast) for the roughness heights and 1 m (four to six times the largest clast) for  
543  
544 224 the grid size used to compute  $\sigma_z$  and  $RMSH$ . The workflow followed to derive a proxy correlation  
545  
546 225 between grain size and surface roughness obtained from UAS-SfM point clouds is summarized in Fig.  
547  
548 226 4.

## 549 227 **4. Results**

### 550 228 *4.1. Roughness as a proxy of GSD percentiles*

551  
552 229 Roughness estimates from SfM were compared to the field grain size measurements. Taking the GPS  
553  
554 230 coordinates of the central point of each Wolman sample area, a 25-m radius buffer was defined on  
555  
556 231 ArcGis. Then, using the UAS-derived orthophoto mosaic, each buffer was clipped defining an area  
557  
558 232 covering the same sedimentary facies sampled in the field. Surfaces corresponding to woody debris were  
559  
560 233 manually excluded from the buffer. Each defined polygon was used as a mask to extract the data from  
561  
562 234 the roughness clouds. The cumulative distributions of the extracted roughness values were computed  
563  
564 235 and the different percentiles were obtained from these distributions.

565  
566 236 The  $D_{50}$  correlates with median roughness values (Fig. 5): statistically significant (95% confidence level)  
567  
568 237 linear correlations were found between the different roughness estimates and the median grain size,  
569  
570 238 except for the  $RMSH$  in the nontruncated case. Roughness heights exhibited the strongest correlation  
571  
572 239 with median grain size, while  $RMSH$  showed the weakest fit. The strength of correlation was higher  
573  
574 240 when using GSDs truncated at <8 mm. Grain size / roughness ratios were around 1:1 with roughness  
575  
576 241 heights, 1:0.5 with  $\sigma_z$ , and between 1:1 and 1:2 with the  $RMSH$ .

577  
578 242 Significant fit was also found between the 84<sup>th</sup> percentiles of roughness distribution and the  $D_{84}$  (Fig. 6).  
579  
580 243 Significant correlations were found with all the roughness metrics (except for  $RMSH$  in nontruncated  
581  
582 244 cases), but the best fit was found again with  $rh$  in the truncated GSD. With the 16<sup>th</sup> percentiles,  
583  
584 245 significant correlations were only found in the truncated GSD with  $rh$  and the  $\sigma_z$  (Fig., 7). Correlation is  
585  
586 246 lacking in the nontruncated GSD for the 16<sup>th</sup> percentile with the three roughness parameters. Yet again,  
587  
588

591  
592  
593 247 for the 16<sup>th</sup> and the 84<sup>th</sup> percentiles, the grain size / roughness ratios are close to 1:1 with roughness  
594  
595 248 heights, 1:1–2 for *RMSH*, and 1:0.5 for  $\sigma_z$ .

597 249 The previous results show that correlation between roughness and grain size is stronger when  
598  
599 250 considering truncated GSD. The random elevation error in our point clouds is 0.7 cm on flat surfaces.  
600  
601 251 As a consequence, the real protrusion and roughness elevation of particles smaller than ~1 cm may be  
602  
603 252 masked by the intrinsic noise of the SfM reconstructions. Then we can be consider that SfM roughness  
604  
605 253 is somehow truncated at the fine terms of the GSD, and this may explain why the correlation is stronger  
606  
607 254 when using the <8-mm truncated GSDs.

#### 608 609 255 *4.2. Sensitivity analysis*

610  
611 256 Several issues should be considered in order to understand how to produce a good proxy correlation  
612  
613 257 between roughness and grain size. These concern the number of samples required to calibrate the  
614  
615 258 regression model, the influence of point cloud density in the strength of the correlation, and whether or  
616  
617 259 not field calibration would be needed after each flight.

618  
619 260 Therefore, one important issue concerns how many pebble counts are required to calibrate the regression  
620  
621 261 model. Using the mean and standard deviation of our Vénéon's roughness data, a log-normal probability  
622  
623 262 distribution of 3000 roughness values was built (considering *rh* as roughness parameter). Later, the  
624  
625 263 regression model correlating *rh* to  $D_{50}$  (regression equation in Fig. 5D) was applied to each *rh* value of  
626  
627 264 the random roughness distribution, and then a matched distribution of 3000 Wolman  $D_{50}$  was derived.  
628  
629 265 To take into account the effect of the uncertainty in our roughness- $D_{50}$  fit, we introduced in these  
630  
631 266 simulated  $D_{50}$ -samples a gaussian random error equal to the residual standard error of our regression  
632  
633 267 model. Afterwards an increasing number of paired *rh*- $D_{50}$  data was randomly selected; and then the  
634  
635 268 regression was repeatedly run to see how the slope coefficients of the regression equation change as a  
636  
637 269 function of sample number. This simulation was repeated 1000 times. The results of the analysis are  
638  
639 270 presented in Fig. 8A: this plot shows a change of slope in the plot around 8-10 samples. Above this  
640  
641 271 number, slope coefficient of the regression converges to the experimental one, and further increases in  
642  
643 272 the number of samples only involve small changes in the slope coefficient of the regression equation.  
644  
645 273 So, 8-10 samples may be considered as an optimum number of Wolman counts required to calibrate the  
646  
647 274 roughness-grain size fit.

650  
651  
652 275 Later, the influence of point density in the strength of the roughness-grain size fit was also assessed. The  
653  
654 276 point clouds were resampled at different point densities and tested how the  $R^2$  of the regression model  
655  
656 277 varies with point cloud density. Fig. 8B shows how the strength of the regression decreases quickly  
657  
658 278 below average point densities around 10–15 points/m<sup>2</sup>.  
659  
660 279 Finally, we also evaluated whether the calibration between roughness height and grain size is flight  
661  
662 280 dependent or not. Data from the first UAS survey (April) were compared with data obtained during the  
663  
664 281 last survey (July): no differences were observed in the regression lines between April and June; and the  
665  
666 282 data from the five UAS flights plot close to both regression lines, independently of the date of the drone  
667  
668 283 survey (Fig. 9A). This suggests that the calibration is not flight dependent. To check this impression  
669  
670 284 more quantitatively, the regression was run individually for each UAS flight data, and the obtained fit  
671  
672 285 was applied to predict grain size for the other four UAS flight subsamples. Predicted  $D_{50}$  were plotted  
673  
674 286 versus the measured  $D_{50}$  (Fig. 9B) and the plots project very close to the  $x = y$  line. This suggests how  
675  
676 287 well the regression equation obtained for each drone flight predicts the grain size-roughness fit in not  
677  
678 288 overlain areas, at least in those covered by the other four UAS flights. This also involves the shape of  
679  
680 289 the regression, which is not substantially different between the five drone flights.

#### 681 290 *4.3. Applications of the method: mapping surficial GSD and detecting changes after flow events*

##### 683 291 *4.2.1. GSD mapping of exposed gravel bars*

685 292 The UAS-SfM point clouds have been used to derive grain size maps based on surface roughness metrics  
686  
687 293 (Fig. 10). Once surface roughness was estimated, we sorted point clouds into regular grids (1×1 m) and  
688  
689 294 assigned to each cell the median roughness value for the points falling into the grid cell. We used  $rh$  as  
690  
691 295 the roughness metric. Then we applied the calibration law between the median roughness and the median  
692  
693 296 grain size, and as a final step we reclassified the size estimates according to the Wentworth grain size  
694  
695 297 scale (Wentworth, 1922).

697 298 In this way, we derived grain size charts for April and June 2015 with 1×1-m grid cells. These maps  
698  
699 299 were not quantitatively validated, but visual assessment revealed that the results were coherent with  
700  
701 300 textures of exposed gravel bars visible on images (Fig. 11). The derived grain size maps are restricted  
702  
703 301 to the exposed gravel bar surfaces, and they exclude the areas of woody debris where surface roughness  
704  
705 302 is not directly related to grain-scale topography. In general, the areal extents of the different grain size

709  
710  
711 303 classes were very similar in April and June (Fig. 12). Nevertheless, the percentage of sand-to-fine  
712  
713 304 gravels and boulders were slightly lower in June, while the areal coverage of medium and coarse gravels  
714  
715 305 was slightly larger. Indeed, differences in GSDs inferred from April and June grain size maps are  
716  
717 306 statistically significant ( $p < 0.01$ , Wilcoxon test).

#### 719 307 *4.2.2. Detection of surficial GSD changes after a flow event*

720  
721 308 Sequential UAS data can be also used to link morphological and textural changes following floods. Two  
722  
723 309 UAS surveys (10 April and 11 June 2015) were used to detect changes after a  $42\text{-m}^3\text{ s}^{-1}$  flow event that  
724  
725 310 occurred between 1 and 7 May 2015 (Fig. 13). During this event, the bar-top channels and some marginal  
726  
727 311 areas of gravel bars were flooded. Various morphological adjustments on the surface of the exposed  
728  
729 312 bars and channel margins were induced by this flow event. These data were used to explore whether the  
730  
731 313 elevation changes were related to roughness adjustments on the surface of gravel bars.

732  
733 314 Grain roughness maps were built from April and June UAS-SfM data. Point clouds were sorted into  
734  
735 315 regular grids ( $1 \times 1$  m), and we assigned to each pixel the median roughness value using the  $rh$  metrics.  
736  
737 316 Then, by subtracting the April and June roughness grids, a map of surficial roughness change was  
738  
739 317 produced. A level of detection was applied to the map using the following equation for error estimation:

$$740  
741 318 U = 1.96 \cdot \sqrt{2\sigma^2} \quad (1)$$

742  
743 319 where  $U$  is the uncertainty in roughness change estimation, and  $\sigma$  is the resolution of the SfM point  
744  
745 320 clouds defined from a flat scanned surface (section 3.2.1). Parameter  $U$  was then used as a threshold for  
746  
747 321 roughness change detection. The obtained  $U$  was 19 mm, below the median roughness and average  $D_{50}$   
748  
749 322 of Vénéon gravel bars (31 and 39 mm, respectively). This value was subtracted from all the cells in the  
750  
751 323 model of roughness differences to derive a map of significant roughness change (Fig. 14). An average  
752  
753 324 roughness variation of  $-1.6$  mm (standard deviation, 36.0 mm) was obtained.

754  
755 325 To better evaluate the detected roughness adjustments, these should be compared with morphological  
756  
757 326 changes (Fig. 14). The use of sequential 3D data sets to evaluate geomorphological changes requires  
758  
759 327 multitemporal point cloud alignment (Lallias-Tacon et al., 2014). An alignment operation was  
760  
761 328 performed between the April and June point clouds with the automatic iterative closest point (ICP)  
762  
763 329 algorithm from Cloud Compare by selecting common stable surfaces. This method is often used for

768  
769  
770 330 alignment of adjacent scans of terrestrial and airborne LiDAR (Lallias-Tacon et al., 2014) and  
771  
772 331 sometimes for fusion of airborne and terrestrial LiDAR point clouds (Iavarone and Vagners, 2003;  
773  
774 332 Rabatel et al., 2008; Theule et al., 2012). After the alignment process, the average difference in elevation  
775  
776 333 between common stable areas was 1 mm.

777  
778 334 Based on the recorded point clouds, DEMs were constructed with ArcGIS following a simple workflow  
779  
780 335 in which ground points and inverse weighted distances were used to derive a triangular irregular network  
781  
782 336 (TIN), which was then linearly resampled on a 0.25-m grid. A DEM of differences (DoD) was calculated  
783  
784 337 by subtracting the June elevations from April elevations on a cell-by-cell basis. Several studies (Heritage  
785  
786 338 et al., 2009; Wheaton et al., 2010; Milan et al., 2011) have demonstrated the importance of accounting  
787  
788 339 for spatially distributed errors across a DEM surface. Spatially distributed errors were accounted here  
789  
790 340 following the protocol suggested by Lallias-Tacon et al. (2014), based on Milan et al. (2011). This  
791  
792 341 procedure estimates spatially distributed errors in the DoD by separating errors induced by the  
793  
794 342 photogrammetric survey and errors induced by interpolation method used to produce the DEM. The  
795  
796 343 level of detection (LoD) of altimetric change can then be propagated into the DoD from:

$$797 \quad 344 \quad LoD = 1.96 \cdot \sqrt{\left(\sqrt{\sigma_{sur\ Avril}^2 + \sigma_{int\ Avril}^2}\right)^2 + \left(\sqrt{\sigma_{sur\ June}^2 + \sigma_{int\ June}^2}\right)^2} \quad (2)$$

799 345 where  $\sigma_{sur}$  is the altimetric error and  $\sigma_{int}$  the interpolation error. As already pointed out in section 3.2.1,  
800  
801 346 the altimetric error (5.3 cm) was estimated from the comparison with dGPS data. Interpolation errors  
802  
803 347 were estimated from a regression equation established between the standard deviation of elevation error  
804  
805 348 (difference between SfM points and DEM pixel elevations) and topographic roughness. Equation (2)  
806  
807 349 defines the minimum LoD for a significant elevation change between April and October.

809 350 The thresholded DoD shows an average elevation change of 5 cm (standard deviation,  $\pm 25$  cm). Patches  
810  
811 351 of scour and fill are spread throughout the surface of compound bars, covering roughly 30% of the  
812  
813 352 exposed surface (9% scour, 21% fill). The thresholded DoD was compared to the model of roughness  
814  
815 353 variations (Fig. 14). While different directions of change in grain roughness were found for the scoured  
816  
817 354 and filled surfaces, scoured areas show some tendency toward roughness decrease (average change,  
818  
819 355  $-19.4$  mm,  $\pm 49.5$  mm). Eroded surfaces were often located on bar platforms, where scouring involved  
820  
821 356 the removal of protruding stones as well as smoothing of sand patches through removal of bedforms  
822  
823 357 (current ripples, megaripples). This should involve a decrease in surface roughness.

827  
828  
829 **358 5. Discussion**

830  
831 **359 5.1. Roughness as a proxy of GSD**

832  
833 **360** These results show that the *rh* roughness metric provided the best proxy of grain size percentiles.  
834  
835 **361** Compared to the  $\sigma_z$  and the *RMSH*, roughness heights are more closely related to the actual protrusion  
836  
837 **362** of grains on the bed surface: it quantifies the exact difference in height between the top of stones and  
838  
839 **363** the average bed surface, while  $\sigma_z$  and the *RMSH* only deliver an averaged measure of grain scale relief  
840  
841 **364** in the surrounding area of each stone.

842  
843 **365** In some of the sample locations, sand and fine sediment occupies pockets between coarse stones. This  
844  
845 **366** strong variation in local relief in these interstitial spaces involves high roughness values for the smaller  
846  
847 **367** clasts. Also, sand bodies in the Vénéon are often featured by bedforms (current ripples, megaripples),  
848  
849 **368** so roughness is more closely related to microforms than to grains in some of these sand patches. Both  
850  
851 **369** effects may help to explain why correlation strength decreases for the finer percentiles of the GSDs.

852  
853 **370** The comparison with previously published TLS-based experiments (Fig. 15) reveals that no universal  
854  
855 **371** relation exists between surface roughness and grain size. Our results fall very close to a 1:1 ratio and  
856  
857 **372** very close to the *c*-axis plot reported by Heritage and Milan (2009). However, with the Wolman  
858  
859 **373** sampling, the *b*-axis was measured. It is often said (Johansson, 1963; Limerinos, 1970; Bathurst, 1982;  
860  
861 **374** Gomez, 1993) that the *c*-axis is usually aligned to the vertical, while the *a*- and *b*-axes are preferentially  
862  
863 **375** aligned orthogonal and parallel to the main flow direction, respectively (Gomez, 1993; Baewert et al.,  
864  
865 **376** 2014). Visual assessment in the field of particle shape revealed that clasts are mostly rounded to sub-  
866  
867 **377** rounded in the Vénéon. Rounded particles are featured by very similar *c*- and *b*-axis dimensions, and  
868  
869 **378** this could explain why the data plot very close to a 1:1 ratio and also to the *c*-axis roughness relations  
870  
871 **379** found by Heritage and Milan (2009). Brasington et al. (2012) plotted data between the *c*- and *b*-axis  
872  
873 **380** relation given by Heritage and Milan (2009), which could be partially explained by the fact that their  
874  
875 **381** data set includes a mixture of rounded and platy particles. In the same vein, Heritage and Milan (2009)  
876  
877 **382** found that two patches of similar size and particle shape may have different roughness heights resulting  
878  
879 **383** from textural differences. Apart from clast shape, other textural constraints on surface roughness may  
880  
881 **384** be packing, variable burial depth of clasts by fines or imbrication angle (Robert, 1990; Heritage and  
882  
883 **385** Milan, 2009; Hodge et al., 2009b), as well as bedforms and particle clusters (Brasington et al., 2012).  
884  
885

886  
887  
888 386 In summary, while grain size should be one of the major controls on surface roughness in gravel-bed  
889  
890 387 rivers (Hodge et al., 2009b), other factors such as particle shape, grain packing, imbrication, and  
891  
892 388 clustering are also important controls on surface roughness. As a consequence, the grain size–roughness  
893  
894 389 relationship is far from being universal. In each study case, it should be affected in a unique manner by  
895  
896 390 all the textural constraints.

### 898 391 *5.2. GSD mapping of exposed gravel bars*

899  
900 392 Based on UAS-SfM point clouds and using surface roughness metrics, we succeeded in deriving grain  
901  
902 393 size charts of the study site. While these maps were not validated with an independent data set, the visual  
903  
904 394 comparison with high-resolution images (2-cm pixel size) suggests that these GSD charts are quite  
905  
906 395 realistic when compared with the actual surface GSD of gravel bars.

907  
908 396 Comparable spatially continuous grain size maps were previously produced based on high-resolution  
909  
910 397 aerial images and image texture analysis (Carbonneau et al., 2005; Verdu et al., 2005; Dugdale et al.,  
911  
912 398 2010; de Haas et al., 2014; Tamminga et al., 2014). This method can potentially deliver continuous grain  
913  
914 399 size maps over large areas (1–80 km) with centimetric precision at spatial resolutions of 1 m<sup>2</sup>. However,  
915  
916 400 it is strongly dependent on particle sorting, substrate homogeneity, and scene illumination and requires  
917  
918 401 very high resolution imagery (Brasington et al., 2012). Indeed, the image texture approach is adversely  
919  
920 402 affected by the blurred imagery often acquired from relatively unstable UAS platforms (de Haas et al.,  
921  
922 403 2014; Woodget, 2015). On the contrary, the SfM-roughness approach allows more flexibility on data  
923  
924 404 acquisition, and it also has the potential to provide grain size measurements at finer scales than the image  
925  
926 405 texture analysis, which is restricted by the pixel size of available aerial imagery and pixel bleeding  
927  
928 406 effects when the operator calibrates directly on the aerial images (Dugdale et al., 2010). Additionally,  
929  
930 407 UAS-SfM simultaneously provides highly accurate topographic reconstructions and GSD information  
931  
932 408 of gravel beds, while the image texture approach only delivers grain size information.

933 409 However, GSD mapping based on UAS-SfM data sets has two main limitations. One is because of  
934  
935 410 woody debris on gravel bars. On these surfaces, roughness is not related to grain size, but rather to the  
936  
937 411 shape of the log and woody bodies. No grain size information can be retrieved from roughness near  
938  
939 412 these areas. Another disadvantage is the limitation of our GSD charts to exposed gravel bar surfaces.  
940  
941 413 This could be enough for many applications, but in other cases the grain size of submerged areas is also

945  
946  
947 414 important. One possible solution is the combination of the UAS-SfM-based method with the  
948  
949 415 conventional Wolman sampling of submerged areas. Nevertheless, Woodget et al. (2015) showed that  
950  
951 416 a refraction correction could be applied on submerged areas on SfM point clouds, and in this way, they  
952  
953 417 obtained information on channel bathymetry in shallow and clear water areas (<0.5 m) with centimetric  
954  
955 418 vertical accuracy comparable to dry bar areas.

956  
957 419 While we flew over the Vénéon during overall low-flow conditions, the waters of this river were featured  
958  
959 420 by a characteristic opaque, turquoise color typical of glacier melting flows. Consequently, the  
960  
961 421 information about the submerged areas was lost here. However, results from Woodget et al. (2015) are  
962  
963 422 very promising and suggest that the roughness estimates based on UAS-SfM point clouds could also be  
964  
965 423 applied to shallow, clear water areas.

### 966 424 *5.3. Detection of roughness adjustments*

967  
968 425 The level of detection of significant surface roughness change was estimated at 19 mm. Taking into  
969  
970 426 account that the median grain roughness for Vénéon gravel bars is 31 mm, changes that are smaller than  
971  
972 427 the median roughness of gravel bars can be detected with confidence.

973  
974 428 In addition, grain roughness change detection in the Vénéon is only possible for the areas that remained  
975  
976 429 exposed before and after the flow event. Information on underwater GSD changes are lost. However, as  
977  
978 430 we stated above (section 5.2), the results of the Woodget et al. (2015) study suggested that SfM has the  
979  
980 431 potential to be applied to shallow-water submerged areas.

981  
982 432 Milan et al. (2009) and Milan and Heritage (2012) were the first to show grain roughness change maps  
983  
984 433 derived from TLS data. They found coarsening in areas of scour and fining in areas of deposition.  
985  
986 434 Conversely, results of the present study show that morphological and roughness changes are not clearly  
987  
988 435 related. Grain roughness changes occurred in the Vénéon without significant elevation changes and vice-  
989  
990 436 versa. Previously, Rice and Church (2010) also found slight grain size adjustments after floods in the  
991  
992 437 wandering Fraser River, with no clear relation between morphological and grain size changes.

### 993 438 *5.4. Summary recommendations*

994  
995 439 Figure 4 graphically summarizes the workflow followed in this study to approach grain size from surface  
996  
997 440 roughness and UAS-SfM point clouds. The results are very encouraging. Applying SfM-MVS  
998  
999 441 photogrammetry to optical images, taken with a low-cost unmanned aerial platform provided with an

1004  
1005  
1006 442 inexpensive camera system and flown at a low altitude, we succeeded in obtaining a good regression  
1007  
1008 443 model correlating surface roughness and grain size.  
1009  
1010 444 Related to flight conditions, previous studies by Micheletti et al. (2014) and Smith and Vericat (2015)  
1011  
1012 445 showed that a ratio of 1:625 to 639 exists between the RMSE of elevation values and flight range.  
1013  
1014 446 Consequently, strong decreases could be expected in the quality of the roughness reconstruction with  
1015  
1016 447 flight range. Taking this into account, UAS flights should probably be done at low altitudes (30–50 m)  
1017  
1018 448 for surface roughness characterization. The sensor utilized for measurements could also have some  
1019  
1020 449 influence, but this topic is not addressed herein. Probably, the use of a higher-resolution and better-  
1021  
1022 450 quality camera system would allow increasing flight height. Nevertheless, according to Micheletti et al.  
1023  
1024 451 (2015) and Smith et al. (2016), no significant differences in the quality of SfM reconstructions should  
1025  
1026 452 be expected between different sensors flown at flight ranges <100 m. Regarding data processing, it  
1027  
1028 453 seems that point densities between 15 and 20 points/m<sup>2</sup> are enough for a good characterization of surface  
1029  
1030 454 roughness for the purpose of grain size mapping. Once high-density SfM point clouds are derived, they  
1031  
1032 455 can be thinned and density lowered to 15–20 points/m<sup>2</sup>, simply to reduce computing time when  
1033  
1034 456 estimating roughness statistics. This density threshold may be grain size dependent and probably higher  
1035  
1036 457 in case of gravel beds much finer than those studied here.  
1037  
1038 458 From our data, roughness height was found to be the best proxy for grain size. More data is needed to  
1039  
1040 459 determine if roughness height performs the best for all sediment textures. Additionally, it seems that a  
1041  
1042 460 textural signature exists in the slope coefficient of the regression equation linking surface roughness to  
1043  
1044 461 grain size. Field calibration is necessary if SfM roughness is to be used to predict grain size. An  
1045  
1046 462 important issue concerns the minimum number of samples needed to reach a satisfactory regression  
1047  
1048 463 model. Here we used 19 Wolman counts to calibrate the regression models, but according to the  
1049  
1050 464 sensibility analysis, half this number (9 to 10 samples) would have been enough to achieve a reliable fit.  
1051  
1052 465 This is an affordable number of samples, which could easily be taken over 1–2 days simultaneously with  
1053  
1054 466 a UAS survey. However, we can easily imagine that the number of samples needed could be influenced  
1055  
1056 467 by grain size heterogeneity and patchiness. Study cases with a more patched bed texture or grain size  
1057  
1058 468 heterogeneity could require a larger number of samples.

## 1059 469 **6. Conclusions**

1063  
1064  
1065  
1066  
1067  
1068  
1069  
1070  
1071  
1072  
1073  
1074  
1075  
1076  
1077  
1078  
1079  
1080  
1081  
1082  
1083  
1084  
1085  
1086  
1087  
1088  
1089  
1090  
1091  
1092  
1093  
1094  
1095  
1096  
1097  
1098  
1099  
1100  
1101  
1102  
1103  
1104  
1105  
1106  
1107  
1108  
1109  
1110  
1111  
1112  
1113  
1114  
1115  
1116  
1117  
1118  
1119  
1120  
1121

470 In this paper, UAS optical imagery and SfM photogrammetry were used to characterize grain roughness  
471 and GSD of a braided reach in the Vénéon River, a gravel-bed stream located in the French Alps. We  
472 showed the potential of this relatively inexpensive method to provide, together with highly dense and  
473 accurate topographical reconstruction of fluvial topography, spatially continuous characterizations of  
474 grain size.

475 The results found here confirms that surface roughness computed from dense and accurate UAS-derived  
476 SfM point clouds can be used to provide data on the distribution of grain roughness for exposed bar and  
477 river bed surfaces. In summary, the results show moderate to strong correlations (0.45-0.90) between  
478 surface roughness and the different percentiles of the truncated GSD and the coarser percentiles of the  
479 nontruncated GSD (Table 2). In general, the correlation was stronger when using roughness heights as  
480 the roughness metric.

481 We believe that the procedure followed here has great potential for simplifying grain size measurements  
482 in gravel-bed rivers by reducing the number of Wolman counts needed to characterize the reach scale  
483 GSD. Field calibration is still necessary, to the extent that surface roughness is not only controlled by  
484 grain size but also by other textural constraints. Nevertheless, a low number (8-10) of Wolman samples  
485 seems to be required; and once the roughness-GSD model for a given stream has been calibrated,  
486 running long-term monitoring of grain size and roughness would be possible without the need for a new  
487 field sampling. Consequently, the methodology presented in this paper offers a reliable and low-cost  
488 solution for the monitoring of the surface texture of exposed gravel bars over stream reaches of a few  
489 kilometers' length.

490 **Acknowledgements**

491 The present work has been possible thanks to the financial support provided by the ACA14-30 grant,  
492 cofounded by the post-doctoral 'Clarín' program-FICYT (Government of the Principality of Asturias)  
493 and the Marie Curie Cofund. This work also benefited from the financial support from EDF and is part  
494 of the ZABR LTER network. We are particularly grateful to Remi Loire and Jean-René Malavoi for  
495 supporting this project. Special thanks should also be made to Marie Vivier, Gullaume Piton, Emmanuel  
496 Thibert, Fred Ousset, Eric Mermin ,and Pascal Tardif for their comments and strong help in the field.

1122  
1123  
1124 497 Finally, we would like to acknowledge editor-in-chief Richard Marston, Basil Gomez, and the three  
1125  
1126 498 anonymous reviewers for their comments that helped to improve the final version of the paper.  
1127

1128 499 **References**  
1129

1130 500 Aberle, J. and Smart, G. M. (2003). The influence of roughness structure on flow resistance in mountain  
1131  
1132 501 streams. *Journal of Hydraulic Research*, 41 (3), 259-269.  
1133

1134 502 Agisoft (2013). Agisoft PhotoScan User Manual: Professional Edition, Version 1.0.0.  
1135

1136 503 Ashworth, P. J. (1996). Channel bar growth and its relations to local flow strength and direction. *Earth*  
1137  
1138 504 *Surface processes and Landforms*, 21, 103-123.  
1139

1140 505 Baewert, H.; Bimböse, M.; Bryk, A.; Rascher, E.; Schmidt, K.-H. and Morche, D. (2014). Roughness  
1141  
1142 506 determination of coarse grained alpine river bed surfaces using terrestrial laserscanning data. *Zeitschrift*  
1143  
1144 507 *für Geomorphologie*, 58, Supplementary Issue 1, 81-95.  
1145

1146 508 Bathurst, J.C. (1982). Theoretical aspects of flow resistance. In: Hey, R.D., Bathurst, J.C., Thorne, C.R.  
1147  
1148 509 (Eds.), *Gravel-bed Rivers*. Wiley, Chichester, pp. 83–105.  
1149

1150 510 Bluck, B. J. (1976). Sedimentation in some Scottish rivers of low sinuosity. *Transactions of the Royal*  
1151  
1152 511 *Society of Edinburgh*, 69, 425-456.  
1153

1154 512 Brasington, J.; Vericat, D. and Rychov, I. (2012). Modeling river bed morphology, roughness, and  
1155  
1156 513 surface sedimentology using high resolution terrestrial laser scanning. *Water Resources Research* 48  
1157  
1158 514 W11519.  
1159

1160 515 Brown, D.C. (1966). Decentering distortion of lenses. *Photogrammetric Engineering* ,32 (3), 444-462.  
1161

1162 516 Bunte, K. and Abt, S.R., (2001). Sampling surface and subsurface particle-size distributions in wadable  
1163  
1164 517 gravel- and cobble-bed streams for analyses in sediment transport, hydraulics and streambed monitoring.  
1165  
1166 518 General Technical Report n° RMRS GTR74, U.S. Department of Agriculture, Forest service, Rocky  
1167  
1168 519 Mountain Research Station, Fort Collins, Colorado, 428 p.

1169 520 Buscombe, D. (2008). Estimation of grain size distributions and associated parameters from digital  
1170  
1171 521 images of sediment. *Sedimentary Geology*, 210, 1-10.  
1172

1173 522 Butler, J.B.; Lane, S.N. and Chandler, J.H. (2001). Automated extraction of grain-size data for gravel  
1174  
1175 523 surfaces using digital image processing. *Journal of Hydraulic Research*, 39, 519–529.  
1176  
1177  
1178  
1179  
1180

- 1181  
1182  
1183 524 Carbonneau, P.E.; Lane, S.N. and Bergeron, N. (2004). Catchment-scale mapping of surface grain size  
1184  
1185 525 in gravel bed rivers using airborne digital imagery. *Water Resources Research* 40, W07202.  
1186  
1187 526 Carbonneau, P.E.; Bergeron, N. and Lane, S.N. (2005). Automated grain size measurements from  
1188  
1189 527 airborne remote sensing for long profile measurements of fluvial grain sizes. *Water Resources Research*,  
1190  
1191 528 41, W11426.  
1192  
1193 529 Church, M. (1978). Palaeohydrological reconstructions from a Holocene valley fill. In: Miall, A. (ed.).  
1194  
1195 530 *Fluvial Sedimentology*, Can. Soc. Petrol. Geol. Mem., vol. 5, pp., Alberta (Canada), pp. 743–772.  
1196  
1197 531 CloudCompare (version 2.6.2) [GPL software] (2015). Retrieved from <http://www.cloudcompare.org/>  
1198  
1199 532 de Haas, T. ; Ventra, D. ; Carbonneau, P. and Kleinhans, M.G. (2014). Debris flow dominance of  
1200  
1201 533 alluvial fans masked by runoff reworking and weathering. *Geomorphology*, 217, 165-181.  
1202  
1203 534 Detert, M. and Weitbrecht, V. (2013). User guide to gravelometric image analysis by BASEGRAIN.  
1204  
1205 535 In: *Advances in Science and Research*, S. Fukuoka, H. Nakagawa, T. Sumi, H. Zhang (Eds.), Taylor &  
1206  
1207 536 Francis Group, London, pp. 1789-1795.  
1208  
1209 537 Dietrich, J. T. (2016). Riverscape Mapping with Helicopter-Based Structure-From-Motion  
1210  
1211 538 Photogrammetry. *Geomorphology*, 252, 144–157.  
1212  
1213 539 Dietrich, W. E.; Nelson, P. A.; Yager, E.; Venditti, J. G.; Lamb, M. P. and Collins, L. (2005). Sediment  
1214  
1215 540 patches, sediment supply, and channel morphology. In: Parker, G. and Garcia, M. H. 4<sup>th</sup> Conference on  
1216  
1217 541 River, Coastal, and Estuarine Morphodynamics, RCEM 2005, A. A. Balkema Publishers, Rotterdam,  
1218  
1219 542 pp. 79–90.  
1220  
1221 543 Dugdale, S.; Carbonneau, P. and Campbell, D. (2010). Aerial photosieving of exposed gravel bars for  
1222  
1223 544 the rapid calibration of airborne grain size maps. *Earth Surface Processes and Landforms*, 35, 627-639.  
1224  
1225 545 Entwistle, N.S. and Fuller, I.C. (2009). Terrestrial laser scanning to derive the surface grain size facies  
1226  
1227 546 character of gravel bars. In Heritage, G.L. and Large, A.R.G. (Eds). *Laser Scanning for the*  
1228  
1229 547 *Environmental Sciences*, Wiley-Blackwell, London.  
1230  
1231 548 Fonstad, M. A. ; Dietrich, J.T. ; Courville, B.C. ; Jensen, J.L. and Carbonneau, P.E. (2013). Topographic  
1232  
1233 549 structure from motion: a new development in photogrammetric measurement. *Earth Surface Processes*  
1234  
1235 550 *and Landforms*, 38, 421–430.  
1236  
1237  
1238  
1239

- 1240  
1241  
1242 551 Gomez, B. (1993). Roughness of stable, armored gravel beds. *Water Resources Research*, 29 (11), 3631-  
1243 3642.  
1244 552  
1245  
1246 553 Graham, D.J.; Reid, I. and Rice, S.P. (2005). Automated sizing of coarse-grained sediments: image-  
1247 processing procedures. *Mathematical Geology* 37, 1–28.  
1248 554  
1249  
1250 555 Guerit, L. ; Barrier, L. ; Narteau, C. ; Métivier, F. ; Liu, Y. ; Lajeunesse, E. ; Gayer, E. ; Meunier, P. ;  
1251 Malverti, L. and Ye, B. (2014). The Grain-size Patchiness of Braided Gravel-Bed Streams – example of  
1252 the Urumqi River (northeast Tian Shan, China). *Advances in Geosciences*, 37, 27-39.  
1253 557  
1254 558 Heritage, G. and Milan, D. J. (2009). Terrestrial laser scanning of grain roughness in a gravel bed river.  
1255 *Geomorphology*, 113 (1), 4-11.  
1256 559  
1257  
1258 560 Heritage, G.L., Milan, D.J., G.L., Large, A.R.G., Fuller, I. and Hetherington, D. (2009). Influence of  
1259 survey strategy and interpolation model upon DEM quality. *Geomorphology*, 112, 334-344.  
1260 561  
1261  
1262 562 Hodge, R. A.; Brasington, J. and K. S.Richards (2009a). *In situ* characterization of grain-scale fluvial  
1263 morphology using TLS. *Earth Surface Processes and Landforms*, 34, 954–968.  
1264 563  
1265  
1266 564 Hodge, R. A.; Brasington, J. and K. S.Richards (2009b). Analyzing laser-scanned digital terrain models  
1267 of gravel bed surfaces: Linking morphology to sediment transport processes and  
1268 hydraulics. *Sedimentology*, 56, 2024–2043.  
1269 565  
1270  
1271 566 Hohenthal, J.; Alho, P.; Hyypä, J. and Hyypä, H. (2011). Laser scanning applications in fluvial  
1272 studies. *Progress in Physical Geography* 35 (6), 782-809.  
1273 567  
1274  
1275 568 Iavarone, A. and Vagners, D. (2003). Sensor fusion: generating 3D by combining airborne and tripod  
1276 mounted LIDAR data. *Proceeding of ISPRS workshop on “Visualization and Animation of Reality-  
1277 based 3D Models”*. *Int. Arch. Photogramm. Remote. Sens. Spat. Inf. Sci.* XXXIV (5/W10), 7.  
1278 569  
1279  
1280 570 Ibbeken, H. and Schleyer, R. (1986). Photo-sieving: a method for grain-size analysis of coarse grained,  
1281 unconsolidated bedding surfaces. *Earth Surface Processes and Landforms* 11, 59–77.  
1282 571  
1283  
1284 572 James, M.R. and Robson, S. (2012). Straightforward reconstruction of 3D surfaces and topography with  
1285 a camera: accuracy and geosciences application. *Journal of Geophysical Research* 117, F03017.  
1286 573  
1287  
1288 574 James, M.R. and Robson, S. (2014). Mitigating systematic error in topographic models derived from  
1289 UAV and ground-based image networks. *Earth Surface Processes and Landforms*, 39, 1413-1420.  
1290 575  
1291  
1292  
1293 576  
1294  
1295  
1296  
1297  
1298

1299  
1300  
1301  
1302  
1303  
1304  
1305  
1306  
1307  
1308  
1309  
1310  
1311  
1312  
1313  
1314  
1315  
1316  
1317  
1318  
1319  
1320  
1321  
1322  
1323  
1324  
1325  
1326  
1327  
1328  
1329  
1330  
1331  
1332  
1333  
1334  
1335  
1336  
1337  
1338  
1339  
1340  
1341  
1342  
1343  
1344  
1345  
1346  
1347  
1348  
1349  
1350  
1351  
1352  
1353  
1354  
1355  
1356  
1357

578 Javernick, L.; Brasington, J. and Caruso, B. (2014). Modelling the topography of shallow braided rivers  
579 using Structure-from-Motion photogrammetry. *Geomorphology*, 213, 166-182.

580 Johansson, C.E. (1963). Orientation of pebble clusters in running water. A laboratory study. *Geografiska*  
581 *Annaler*, 45A, 85–112.

582 Lague, D.; Brodu, N. and Leroux, J. (2013). Accurate 3D comparison of complex topography with  
583 terrestrial laser scanner: application to the Rangitikei canyon (N-Z). *Journal of Photogrammetry and*  
584 *Remote Sensing*, 82, 10-26.

585 Lallias-Tacon, S.; Liébault, F. and Piégay, H. (2014). Step by step error assessment in braided river  
586 sediment budget using airborne LiDAR data. *Geomorphology*, 214, 307-323.

587 Lauer, J. W.; Viparelli, E. and Piégay, H. (2016). Morphodynamics and sediment 1D (MAST-1D): 1D  
588 sediment transport that includes exchange with an off-channel sediment reservoir. *Advances in Water*  
589 *Resources*, 93 (A), 135-149.

590 Leopold, L.B.; Wolman, M.G. and Miller, J.P. (1964). *Fluvial Processes in Geomorphology*. WH  
591 Freeman, San Francisco, 522 pp.

592 Limerinos, J. T. (1970). Determination of the Manning coefficient from measured bed roughness in  
593 natural channels. U.S. Geological Survey Water Supply Paper 1898-B.

594 Lisle, T.E. and Madej, M.A. (1992). Spatial variation in armouring in a channel with high sediment  
595 supply. In: *Dynamics of Gravel-bed Rivers* (Eds P. Billi, R.D. Hey, C.R. Thorne and P. Tacconi), pp.  
596 277–293. John Wiley and Sons, London.

597 Micheletti, N.; Chandler, J. H. and Lane, S. N. (2014). Investigating the geomorphological potential of  
598 freely available and accessible structure-from-motion photogrammetry using a smartphone. *Earth*  
599 *Surface Processes and Landforms*, 40 (4), 473-486.

600 Micheletti, N.; Chandler, J. H. and Lane, S. N. (2015). Structure from Motion (SfM) Photogrammetry  
601 Photogrammetric heritage. In: *Geomorphological Techniques*. British Society of Geomorphology, pp.  
602 1-12.

603 Milan, D.J. (2013). Sediment routing hypothesis for pool-riffle maintenance. *Earth Surface Processes*  
604 *and Landforms*, 38, 1623-1641.

1358  
1359  
1360 605 Milan, D.J. and Heritage, G.L. (2012). LiDAR and ADCP use in gravel-bed rivers: Advances since  
1361  
1362 606 GBR6. In Church, M., Biron, P. and Roy, A. (Eds) Gravel-bed Rivers: Processes, Tools, Environments,  
1363  
1364 607 Wiley Blackwell, Chichester.  
1365  
1366 608 Milan, D.J., Heritage, G.L. and Entwistle, N. (2009). Detecting grain roughness change and sorting  
1367  
1368 609 patterns in a gravel-bed river using terrestrial laser scanning. Proceedings of the 33rd IAHR Congress:  
1369  
1370 610 Water Engineering for a Sustainable Environment, Vancouver, Canada August 10-14, 2009. CD-ROM,  
1371  
1372 611 IAHR, pp5004-5011.  
1373  
1374 612 Milan, D.J., Heritage, G.L., Large, A.R.G. and Fuller, I. D. (2011). Filtering spatial error from DEMs;  
1375  
1376 613 implications for morphological change estimation. *Geomorphology*, 125, 160-171.  
1377  
1378 614 Naot, D. (1984). Response of channel flow to roughness heterogeneity. *Journal of Hydraulic*  
1379  
1380 615 *Engineering*, 110, 1568–1587.  
1381  
1382 616 Nelson, P. A.; Venditti, J. G.; Dietrich, W. E.; Kirchner, J. W.; Ikeda, H.; Iseya, F. and Sklar, L. S.  
1383  
1384 617 (2009). Response of bed surface patchiness to reductions in sediment supply. *Journal of Geophysical*  
1385  
1386 618 *Research*, 114, F02005.  
1387  
1388 619 Paola, C. and Seal, R. (1995). Grain-size patchiness as a cause of selective deposition and downstream  
1389  
1390 620 fining, *Water Resources Research*, 31, 1395– 1407.  
1391  
1392 621 Rabatel, A.; Deline, P.; Jaillet, S. and Ravanel, L. (2008). Rock falls in high-alpine rockwalls quantified  
1393  
1394 622 by terrestrial LiDAR measurements: a case study in the Mont Blanc area. *Geophys. Res. Lett.* 35 (10),  
1395  
1396 623 L10502.  
1397  
1398 624 Remondino, F; Spera, M. G.; Nocerino, E.; Menna, F. and Nex, F. (2014). State of the art in high density  
1399  
1400 625 image matching. *The Photogrammetric Record*, 29, 144–166.  
1401  
1402 626 Rice, S. (1995). The spatial variation and routine sampling of spawning gravels in small coastal streams.  
1403  
1404 627 Research Branch, British Columbia Ministry of Forests, Victoria, B.C., Working Paper 06/1995, 41 pp.  
1405  
1406 628 Rice, S.P. and Church, M. (1996). Sampling surficial fluvial gravels: the precision of size distribution  
1407  
1408 629 percentile estimates. *Journal of Sedimentary Research*, 66, 654–665.  
1409  
1410 630 Rice, S. and Church, M. (1998). Grain size along two gravel-bed rivers: statistical variation, spatial  
1411  
1412 631 pattern and sedimentary links. *Earth Surface Processes and Landforms*, 23 (4), 345-363.  
1413  
1414  
1415  
1416

- 1417  
1418  
1419 632 Rice, S. and Church, M. (2010). Grain-size sorting within river bars in relation to downstream fining  
1420  
1421 633 along a wandering channel. *Sedimentology*, 57 (1), 232-251.  
1422  
1423 634 Robert, A. (1990). Boundary roughness in coarse-grained channels. *Progress in Physical Geography*,  
1424  
1425 635 14(1), 42 – 70.  
1426  
1427 636 Robert, A.; Roy, A. G. and Deserres, B. (1992). Changes in velocity profiles at roughness transitions in  
1428  
1429 637 coarse-grained channels. *Sedimentology*, 39, 725–735.  
1430  
1431 638 Robertson, D.P., Cipolla, R. (2009). Structure from Motion. In: Varga, M. (Ed.), *Practical Image*  
1432  
1433 639 *Processing and Computer Vision*. John Wiley, Chichester.  
1434  
1435 640 Rubin, D.M. (2004). A simple autocorrelation algorithm for determining grain size from digital images  
1436  
1437 641 of sediment. *Journal of Sedimentary Research*, 74 (1), 160-165.  
1438  
1439 642 Rychov, I.; Brasington, J. and Vericat, D. (2012). Computational and methodological aspects of  
1440  
1441 643 terrestrial surface analysis based on point clouds. *Computers and Geosciences*, 42, 64-70.  
1442  
1443 644 Semyonov, D., (2011). Algorithms used in Photoscan [Msg 2]. Retrieved May 3. Message posted to  
1444  
1445 645 [www.agisoft.ru/forum/index.php?topic=89.0](http://www.agisoft.ru/forum/index.php?topic=89.0).  
1446  
1447 646 Smart, G.; Aberle, J.; Duncan, M. and Walsh, J. (2004). Measurement and analysis of alluvial bed  
1448  
1449 647 roughness. *Journal of Hydraulic Research*, 42(3), 227-237.  
1450  
1451 648 Smith M.W. and Vericat D. (2015). From experimental plots to experimental landscapes: topography,  
1452  
1453 649 erosion and deposition in sub-humid badlands from Structure-from-Motion photogrammetry. *Earth*  
1454  
1455 650 *Surface Processes and Landforms*, 40 (12), 1656-1671.  
1456  
1457 651 Smith, M. W.; Carrivick, J. L. and Quincey, D. J. (2016). Structure from motion photogrammetry in  
1458  
1459 652 physical geography. *Progress in Physical Geography*.  
1460  
1461 653 Storz-Peretz, Y. and Laronne, J. (2013). Morphotextural characterization of dryland braided channels.  
1462  
1463 654 *Geological Society of America Bulletin*, 125 (9-10), 1599-1617.  
1464  
1465 655 Tamminga, A.; Hugenholtz, C.; Eaton, B. and LaPointe, M. (2014). Hyperspatial remote sensing of  
1466  
1467 656 channel reach morphology and hydraulic fish habitat using an unmanned aerial vehicle (UAV): A first  
1468  
1469 657 assessment in the context of river research and management. *River Research and Applications*, 31 (3),  
1470  
1471 658 379-391.  
1472  
1473 659 Theule, J.I.; Liébault, F.; Loye, A.; Laigle, D. and Jaboyedoff, M. (2012). Sediment budget monitoring  
1474  
1475

1476  
1477  
1478  
1479  
1480  
1481  
1482  
1483  
1484  
1485  
1486  
1487  
1488  
1489  
1490  
1491  
1492  
1493  
1494  
1495  
1496  
1497  
1498  
1499  
1500  
1501  
1502  
1503  
1504  
1505  
1506  
1507  
1508  
1509  
1510  
1511  
1512  
1513  
1514  
1515  
1516  
1517  
1518  
1519  
1520  
1521  
1522  
1523  
1524  
1525  
1526  
1527  
1528  
1529  
1530  
1531  
1532  
1533  
1534

660 of debris-flow and bedload transport in the Manival Torrent, SE France. *Nat. Hazards Earth Syst. Sci.*  
661 12 (3), 731–749.

662 Verdú, J.M.; Batalla, R.J. and Martínez-Casasnovas, J.A. (2005). High-resolution grain-size  
663 characterisation of gravel bars using imagery analysis and geo-statistics. *Geomorphology*, 72, 73-93.

664 Verhoeven, G.; Doneus, M.; Briese, C. and Vermeulen, F. (2012). Mapping by matching: a computer  
665 vision-based approach to fast and accurate georeferencing of archaeological aerial photographs. *Journal*  
666 *of Archaeological Science* 39, 2060–2070.

667 Vericat, D.; Batalla, R. J. and Gibbins, C. N. (2008). Sediment entrainment and depletion from patches  
668 of fine material in a gravel-bed river. *Water Resources Research*, 44.

669 Wentworth, C.K. (1922). A scale of grade and class terms for clastic sediments. *Journal of Geology* 30,  
670 377-392.

671 Westoby, M. J.; Brasington, J.; Glasser, M. J.; Hambrey, M. J.; Reynolds, J. M. (2012). Structure-from-  
672 Motion photogrammetry: a low cost, effective tool for geoscience applications. *Geomorphology* 179:  
673 300–314.

674 Wheaton, J.M., Brasington, J., Darby, S.E. and Sear, D.A. (2010). Accounting for uncertainty in DEMs  
675 from repeat topographic surveys: improved sediment budgets. *Earth Surface Processes and Landforms*  
676 35, 136–156.

677 Wolman, M. G. (1954). A method of sampling coarse river-bed material. *Transactions of the American*  
678 *Geophysical Union*, 35 (6), 951-956.

679 Woodget, A. (2015). Quantifying physical river habitat parameters using high resolution UAS imagery  
680 and SfM photogrammetry. PhD dissertation, University of Worcester. 387 pp.

681 Woodget, A. S. ; Carbonneau, P. E. ; Visser, F. and Maddock, I. P. (2015). Quantifying submerged  
682 fluvial topography using hyperspatial resolution UAS imagery and structure from motion  
683 photogrammetry. *Earth Surface Processes and Landforms*, 40 (1), 47-64.

1535  
1536  
1537  
1538  
1539  
1540  
1541  
1542  
1543  
1544  
1545  
1546  
1547  
1548  
1549  
1550  
1551  
1552  
1553  
1554  
1555  
1556  
1557  
1558  
1559  
1560  
1561  
1562  
1563  
1564  
1565  
1566  
1567  
1568  
1569  
1570  
1571  
1572  
1573  
1574  
1575  
1576  
1577  
1578  
1579  
1580  
1581  
1582  
1583  
1584  
1585  
1586  
1587  
1588  
1589  
1590  
1591  
1592  
1593

**Table 1**

Summary of the main characteristics of the UAS-SfM point clouds

Source/ UAS survey	Point density (pts/m <sup>2</sup> )	Average point distance (cm)	Roughness resolution (cm)
10/04/2015	1052	0.1	0.3
16/04/2015	291	0.8	0.9
11/06/2015	52	3.4	1.3
24/06/2015	45	4.5	-
02/07/2015	36	6.0	0.3
<b>Mean</b>	<b>295</b>	<b>3.0</b>	<b>0.7</b>

1594  
1595  
1596  
1597  
1598  
1599  
1600  
1601  
1602  
1603  
1604  
1605  
1606  
1607  
1608  
1609  
1610  
1611  
1612  
1613  
1614  
1615  
1616  
1617  
1618  
1619  
1620  
1621  
1622  
1623  
1624  
1625  
1626  
1627  
1628  
1629  
1630  
1631  
1632  
1633  
1634  
1635  
1636  
1637  
1638  
1639  
1640  
1641  
1642  
1643  
1644  
1645  
1646  
1647  
1648  
1649  
1650  
1651  
1652

**Table 2.**  $R^2$  for the regression equation fitting roughness and grain size, for several percentiles of the cumulative distributions.

	Nontruncated GSD			Truncated GSD		
	R. heights	$\sigma_z$	RMSH	R. heights	$\sigma_z$	RMSH
<b>D<sub>5</sub></b>	0.08	0.02	0.09	0.59	0.36	0.15
<b>D<sub>16</sub></b>	0.00	0.04	0.00	0.64	0.45	0.19
<b>D<sub>25</sub></b>	0.01	0.04	0.01	0.68	0.58	0.28
<b>D<sub>50</sub></b>	0.26	0.35	0.12	0.89	0.66	0.45
<b>D<sub>75</sub></b>	0.57	0.43	0.22	0.86	0.58	0.32
<b>D<sub>84</sub></b>	0.54	0.35	0.19	0.83	0.51	0.28
<b>D<sub>95</sub></b>	0.35	0.10	0.09	0.73	0.28	0.27

1653  
1654  
1655 **CAPTIONS**  
1656

1657 **Fig. 1.** (A) Location of the study site in France. B) Location of the Vénéon River in the Ecrins Massif  
1658 (French Alps). (C) Detailed view of the study site, with positions of Wolman samples and GCPs.  
1659

1660 **Fig. 2.** Data set of GSD measured in the field during this study. (A) All GSD data. (B) Truncated (<8  
1661 mm) GSD data.  
1662

1663 **Fig. 3.** Steps followed in Agisoft PhotoScan to derive SfM point clouds from UAS imagery.  
1664

1665 **Fig. 4.** Workflow for estimating grain size from UAS-SfM point clouds, using a regression model  
1666 calibrated with a few conventional Wolman pebble counts.  
1667

1668 **Fig. 5.** Median GSD value versus the median roughness value. In the upper row, median GSD values  
1669 are plotted for the nontruncated GSDs; in the lower row, they are plotted for the truncated (<8 mm)  
1670 GSDs.  
1671

1672 **Fig. 6.** GSD 84<sup>th</sup> percentile versus roughness 84<sup>th</sup> percentile. In the upper row, GSD 84<sup>th</sup> percentiles are  
1673 plotted for the nontruncated GSDs; in the lower row, they are plotted for the truncated (<8 mm) GSDs.  
1674

1675 **Fig. 7.** GSD 16<sup>th</sup> percentile versus the roughness 16<sup>th</sup> percentile. In the upper row, GSD 16<sup>th</sup> percentiles  
1676 are plotted for the nontruncated GSDs; in the lower row, they are plotted for the truncated (<8 mm)  
1677 GSDs.  
1678

1679 **Fig. 8.** (A) Results of the analysis concerning how many pebble counts are required to calibrate the  
1680 regression model. An increasing number of roughness- $D_{50}$  data were randomly selected, and then we  
1681 repeatedly ran the regression to analyze how many pebble counts would be required for calibration. In  
1682 the figure, the maximum and minimum values obtained for the slope coefficient of the regression  
1683 equation are plotted (after resampling 1000 times for each sample size). (B) Effect of UAS-SfM point  
1684 cloud density on the correlation coefficient ( $r^2$ ) between grain size and roughness median percentiles.  
1685

1686 **Fig. 9.** (A) Regression fit between the 8-mm lower truncated  $D_{50}$  and the roughness height ( $rh$ ) obtained  
1687 for April (solid line) and July (dashed line) data subsamples. (B) Predicted vs. observed  $D_{50}$  values.  
1688

1689 **Fig. 10.** Workflow for extracting the grain size maps from the UAS-SfM point clouds.  
1690

1691 **Fig. 11.** Surface GSD chart derived from UAS-SfM point clouds (right). Left, the ortophotograph (2-  
1692 cm pixel size). Visual inspection shows correspondence between GSD chart and ortophotograph.  
1693

1694 **Fig. 12.** Areal extent of the different grain size classes determined from surface GSD charts.  
1695  
1696  
1697  
1698  
1699  
1700  
1701  
1702  
1703  
1704  
1705  
1706  
1707  
1708  
1709  
1710  
1711

1712  
1713  
1714 **Fig. 13.** Discharge record of the Vénéon River during the period including UAS flights and grain size  
1715 field sampling. The arrows represent the dates of UAS surveys, and the grey dashed lines represent the  
1716 period during which Wolman pebble counts were done.  
1717  
1718

1719 **Fig. 14.** DoD model (right) and model of roughness changes (left) built for the study site.  
1720

1721 **Fig. 15.** Roughness and grain size data obtained in the current study are compared to TLS data compiled  
1722 from the scientific literature. (A) Comparison with studies that used the standard deviation of elevation  
1723 as the roughness descriptor; (B) comparison with data sets that used the detrended standard deviation.  
1724  
1725  
1726  
1727  
1728  
1729  
1730  
1731  
1732  
1733  
1734  
1735  
1736  
1737  
1738  
1739  
1740  
1741  
1742  
1743  
1744  
1745  
1746  
1747  
1748  
1749  
1750  
1751  
1752  
1753  
1754  
1755  
1756  
1757  
1758  
1759  
1760  
1761  
1762  
1763  
1764  
1765  
1766  
1767  
1768  
1769  
1770

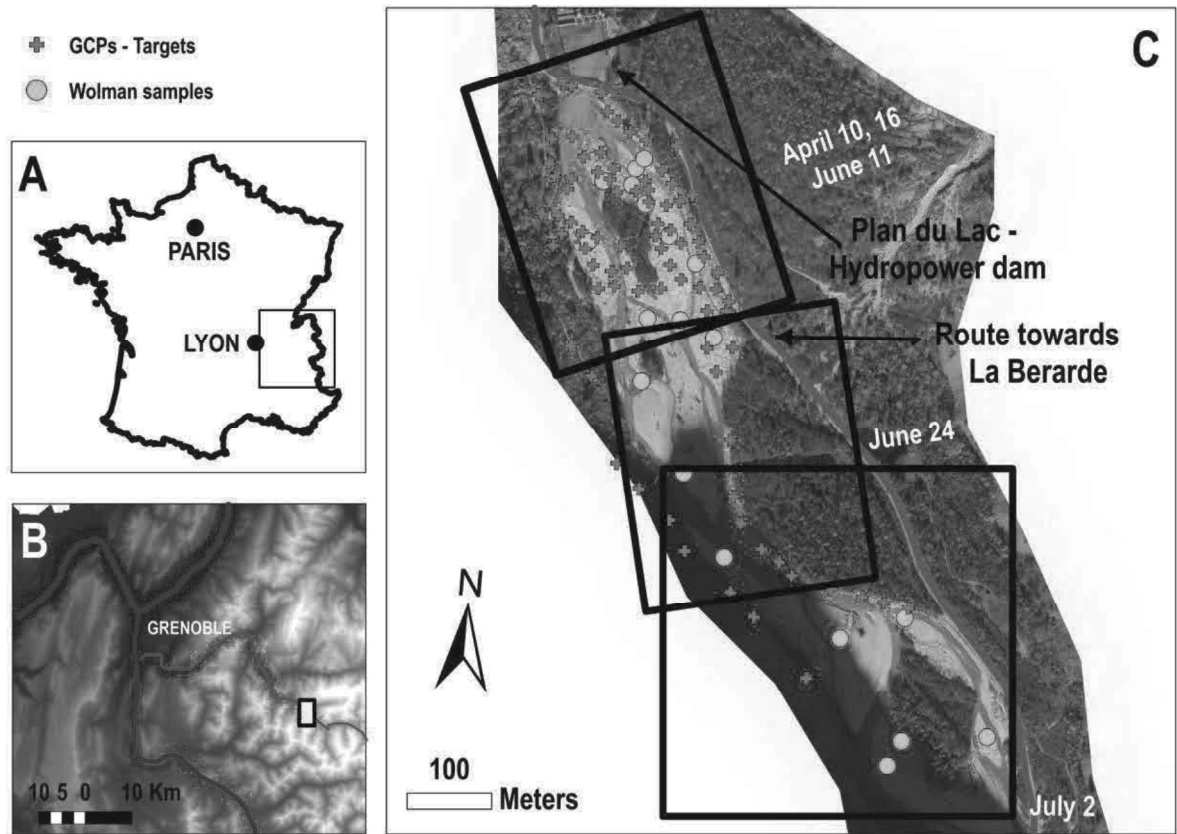


*Figure 1.*

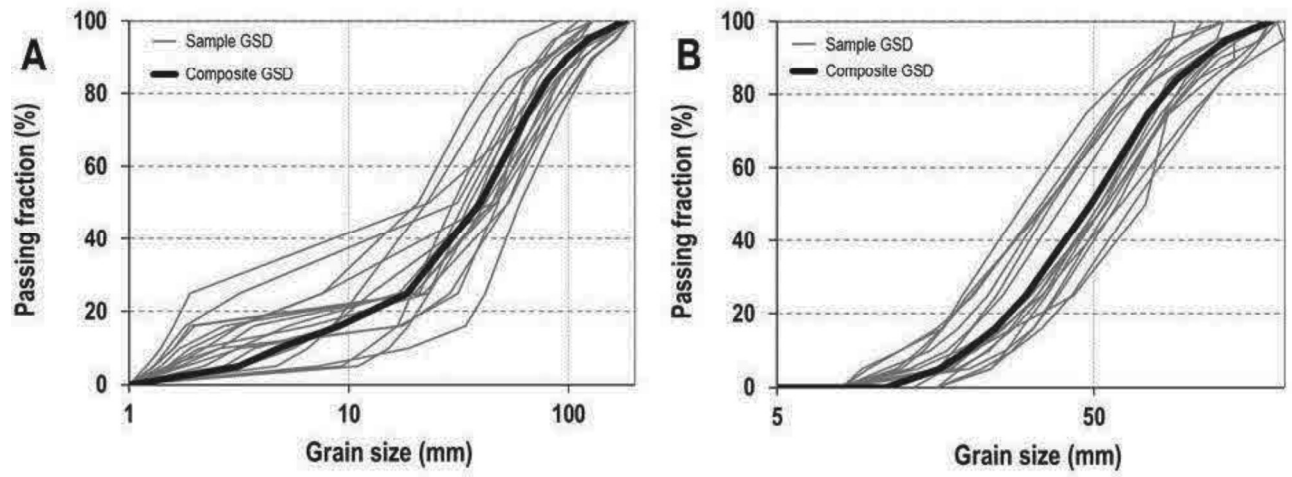


Figure 2.

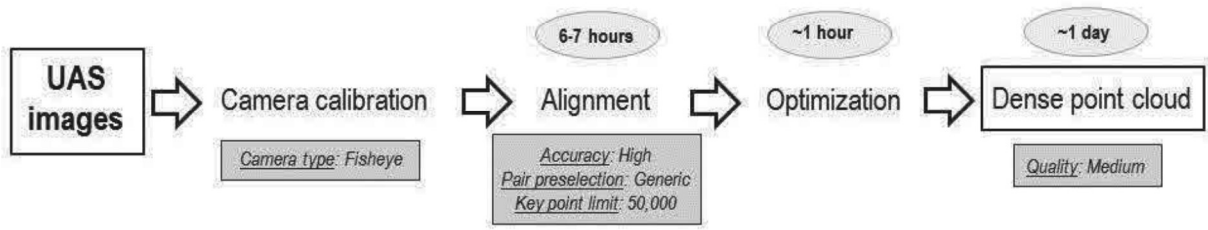
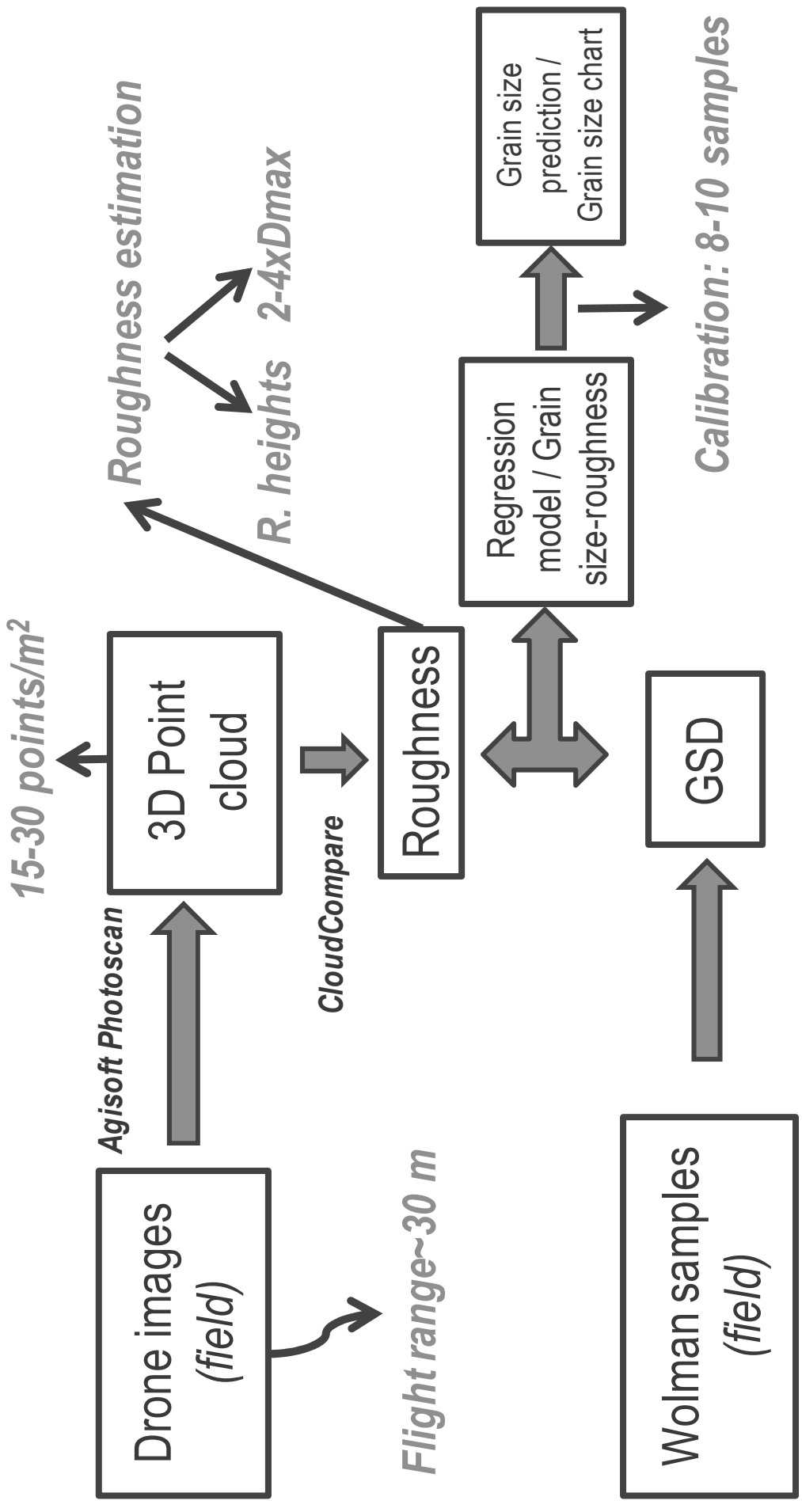
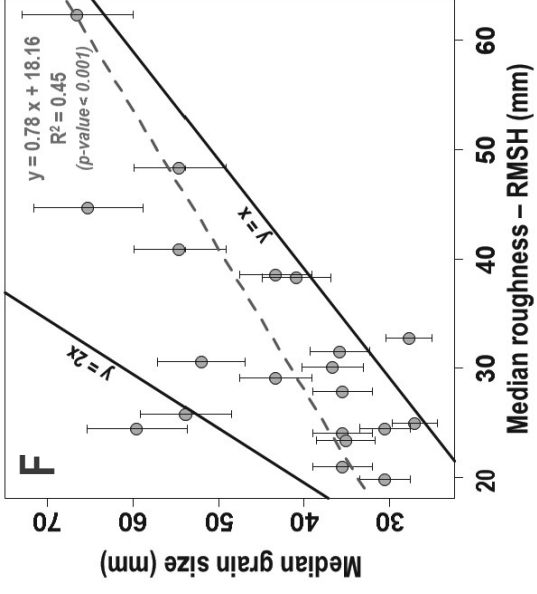
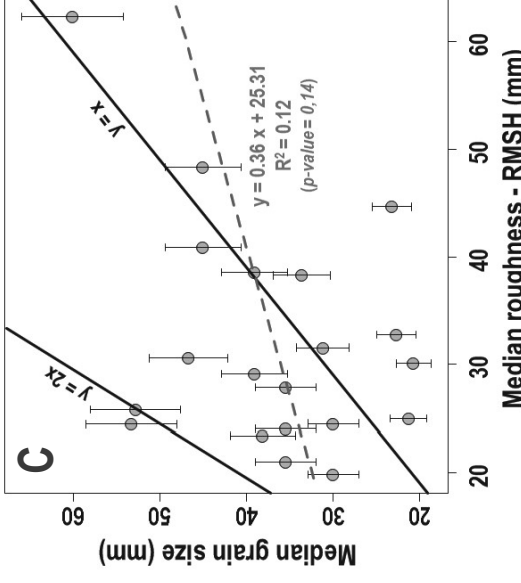
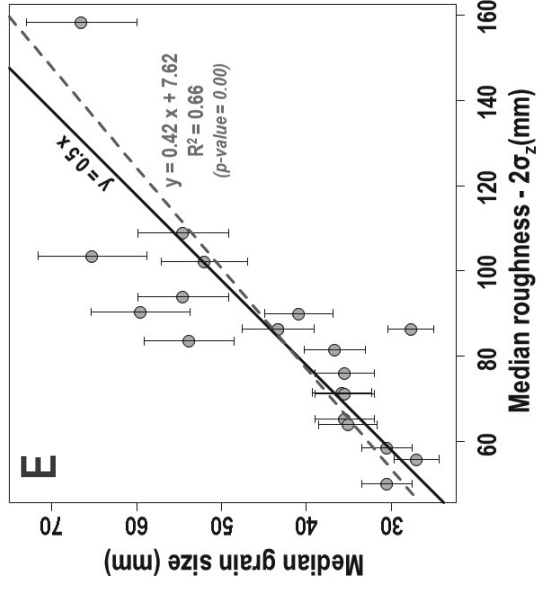
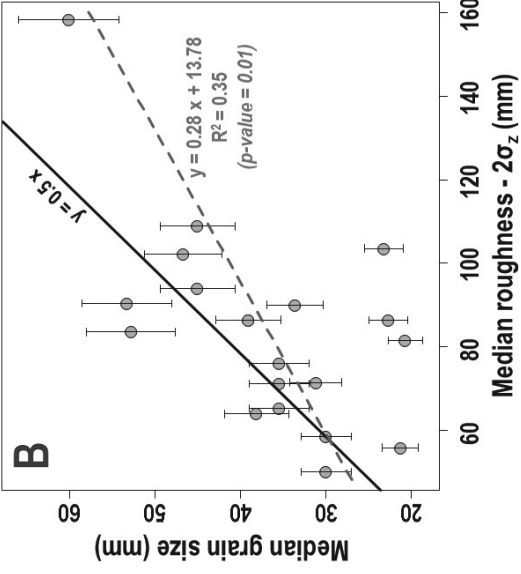
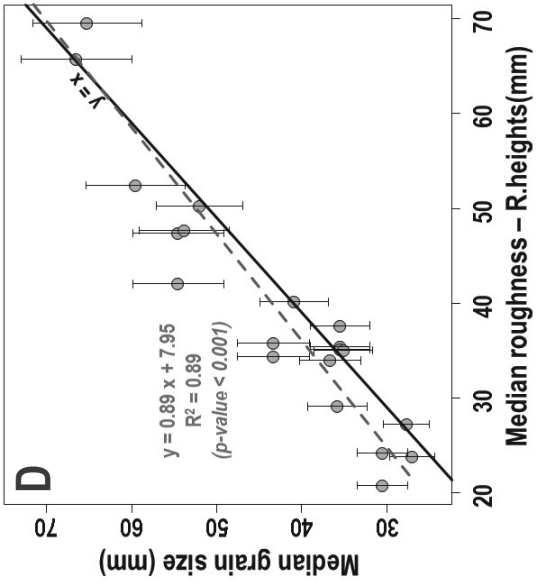
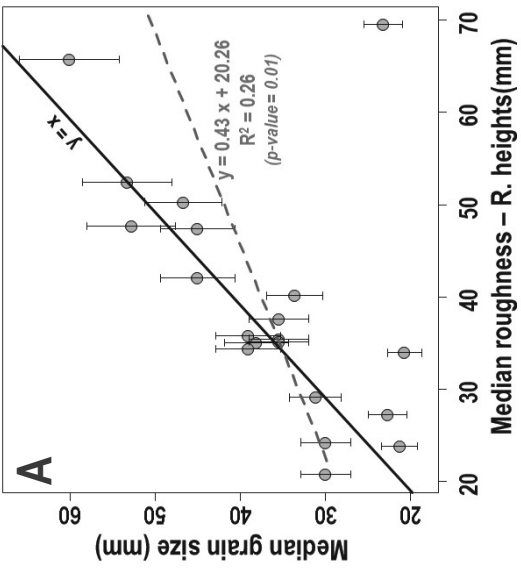
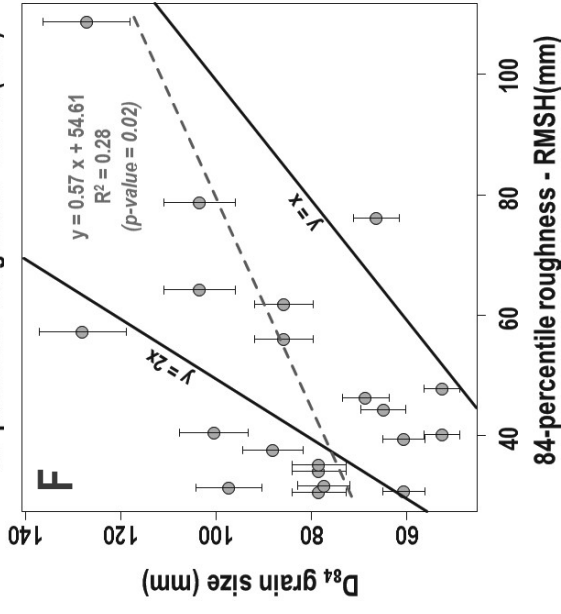
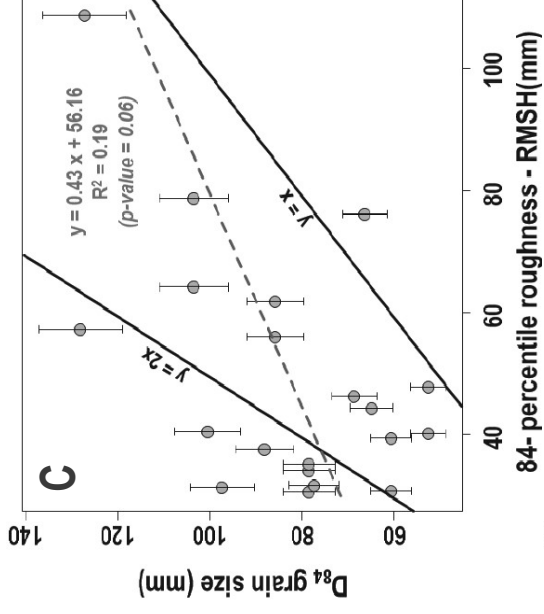
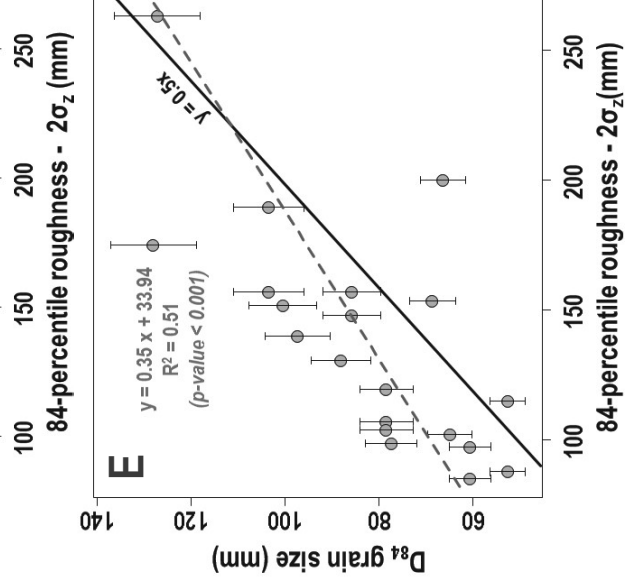
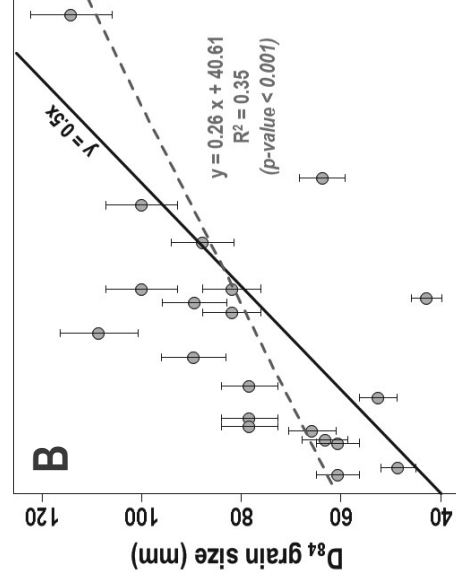
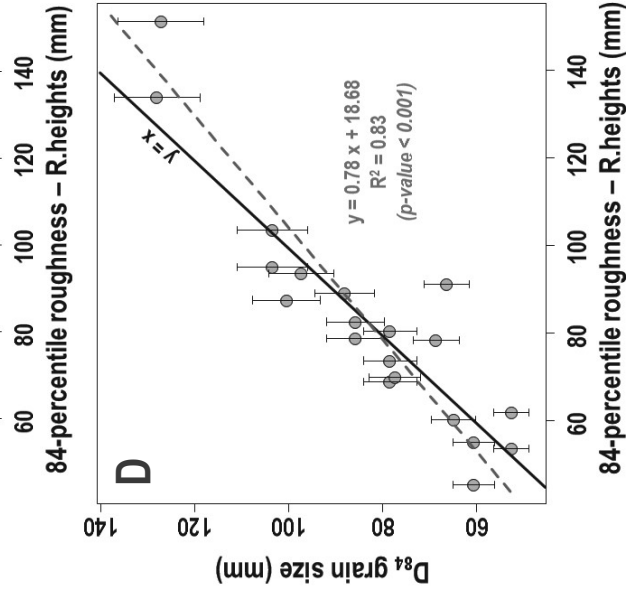
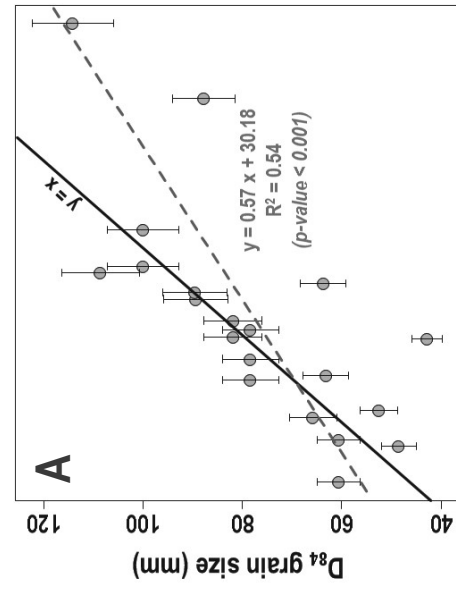
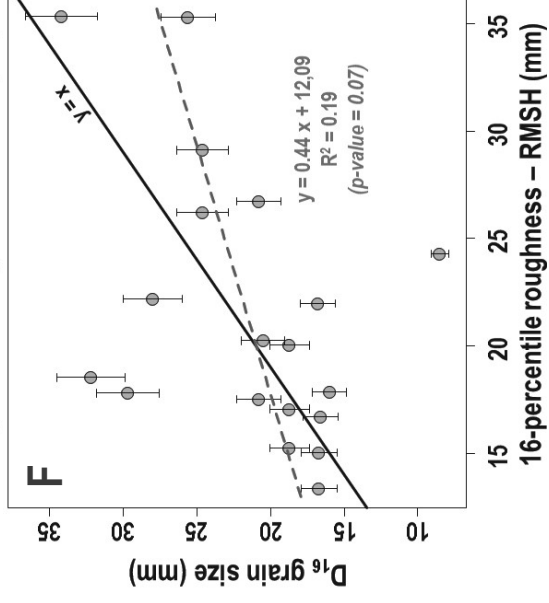
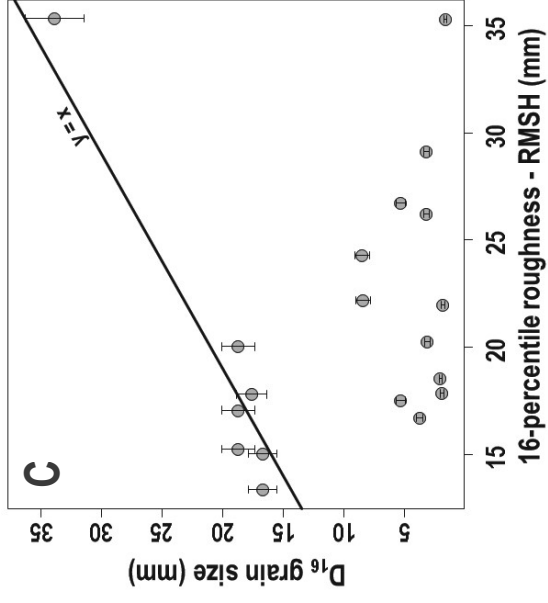
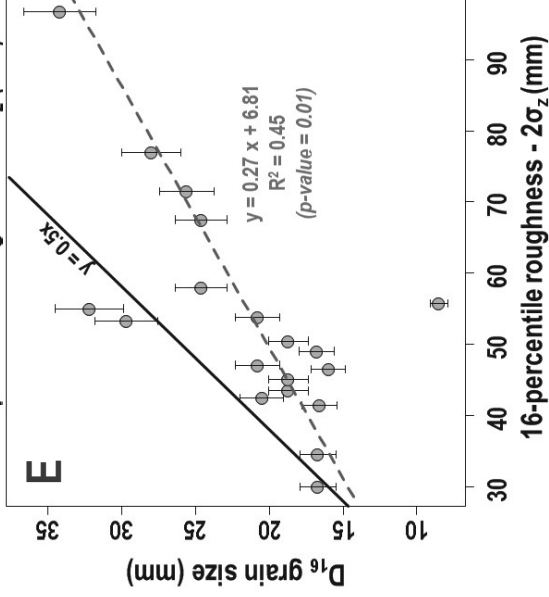
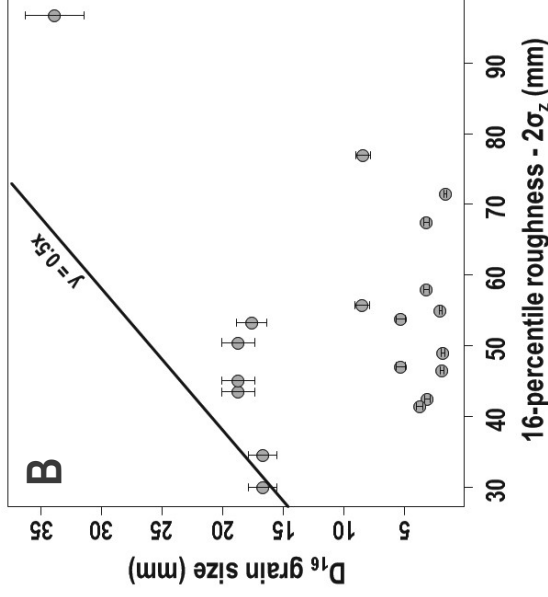
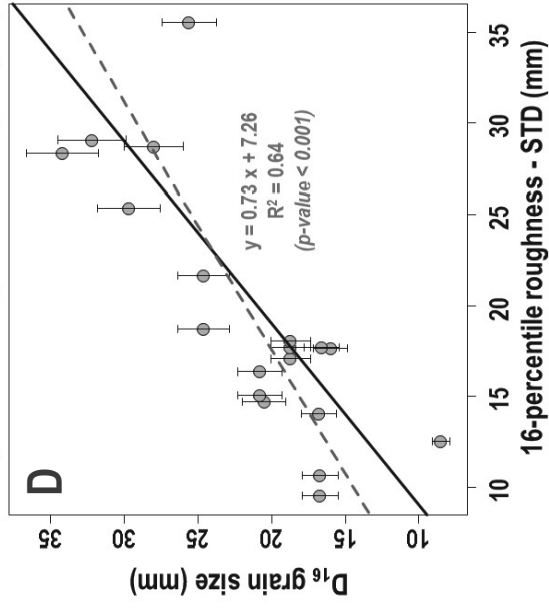
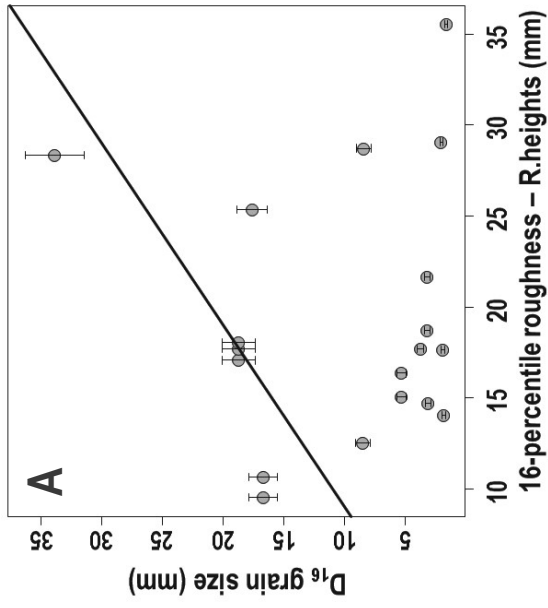


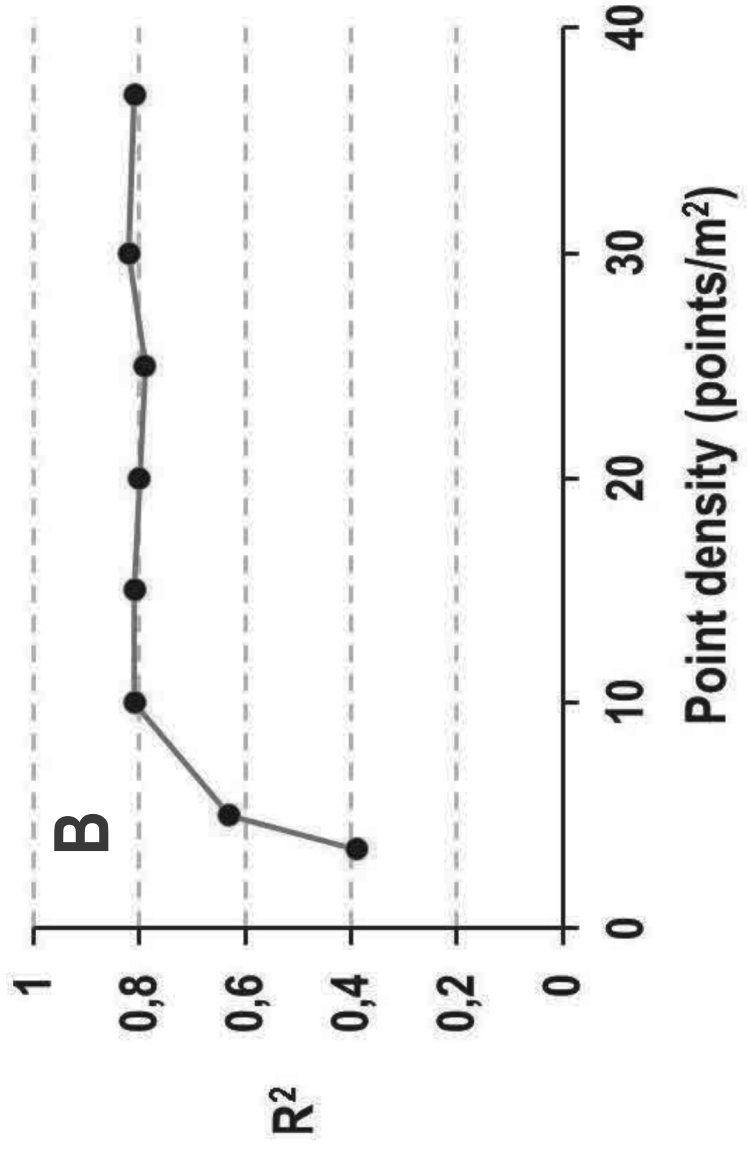
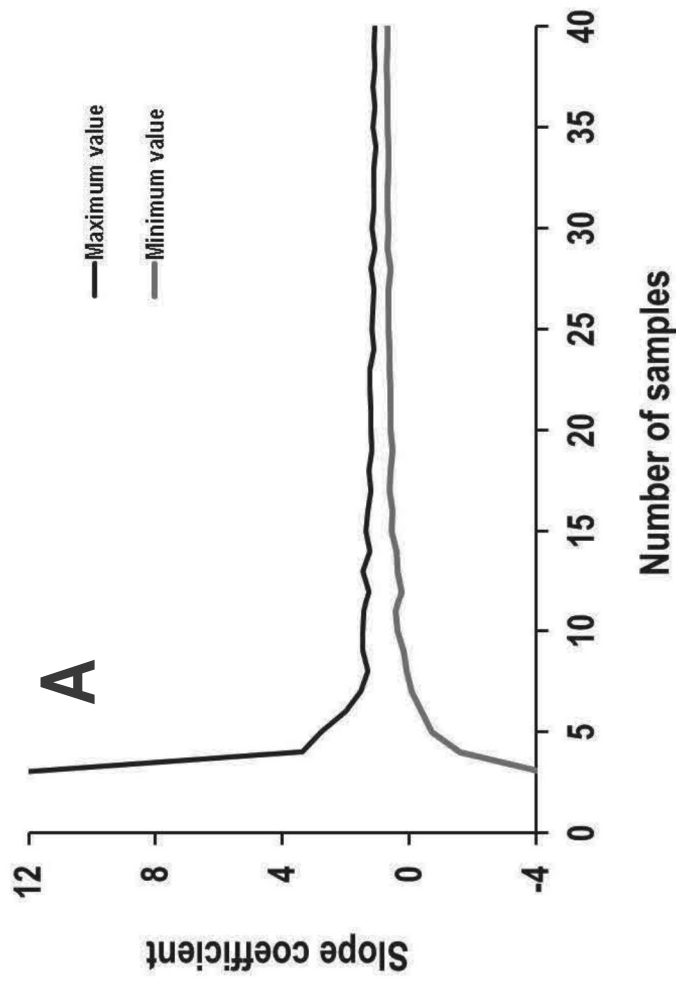
Figure 3

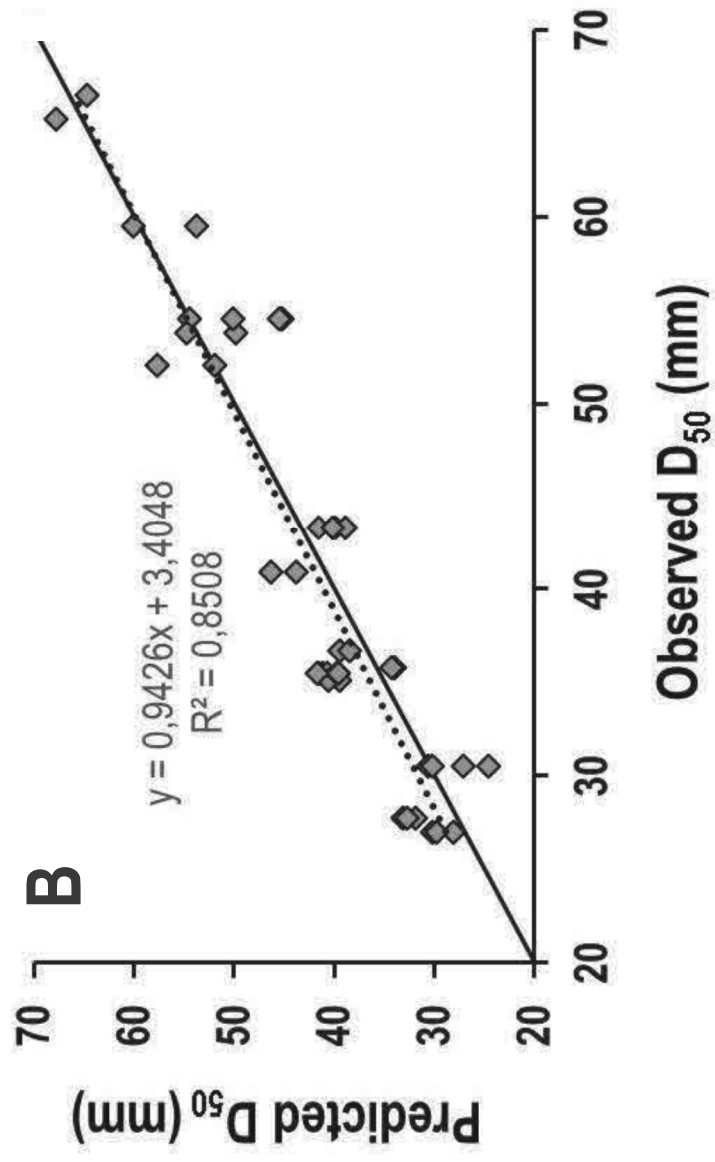
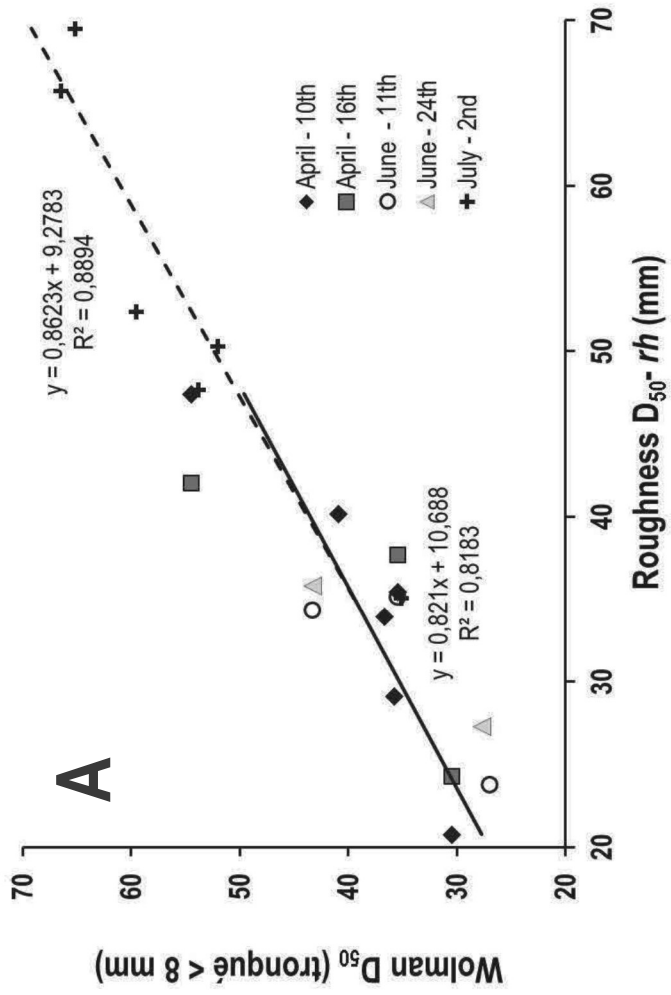












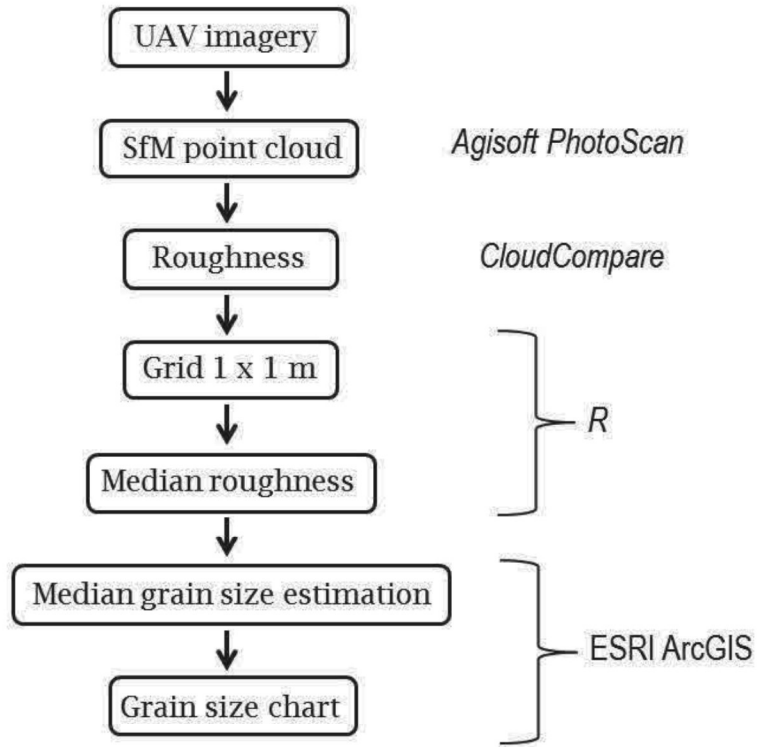


*Figure 10*

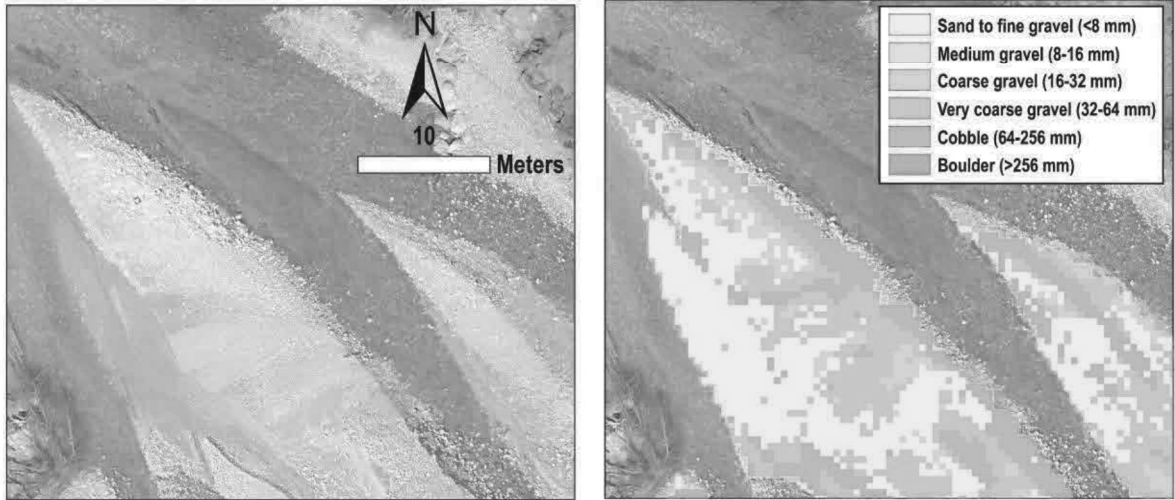


*Figure 11*

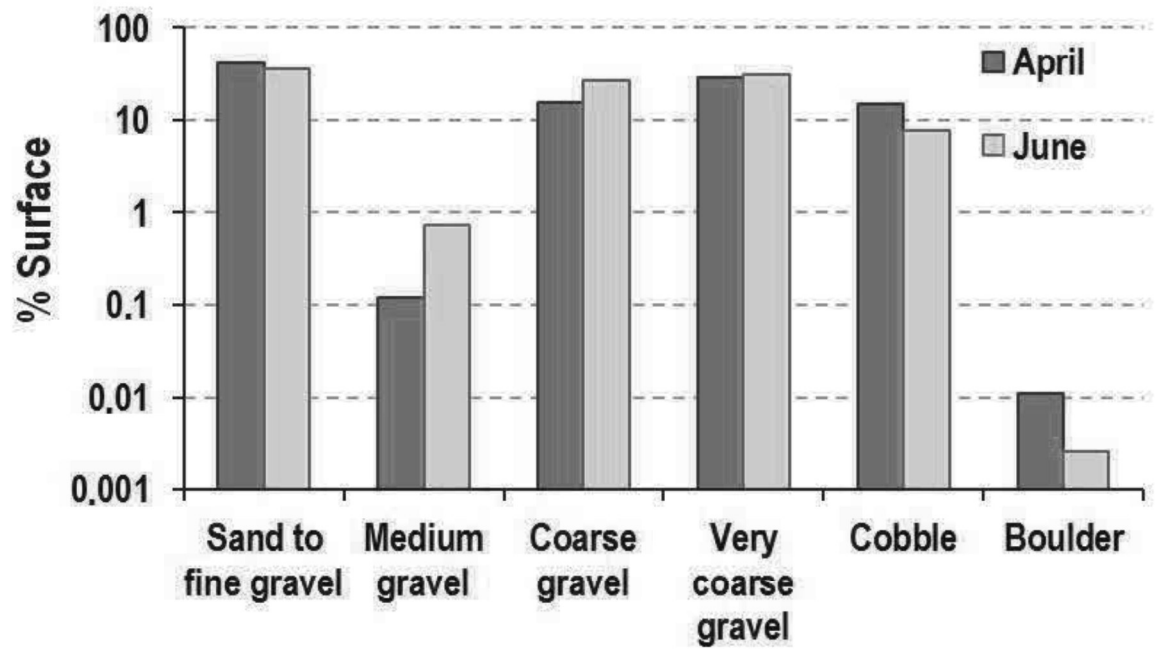


Figure 12

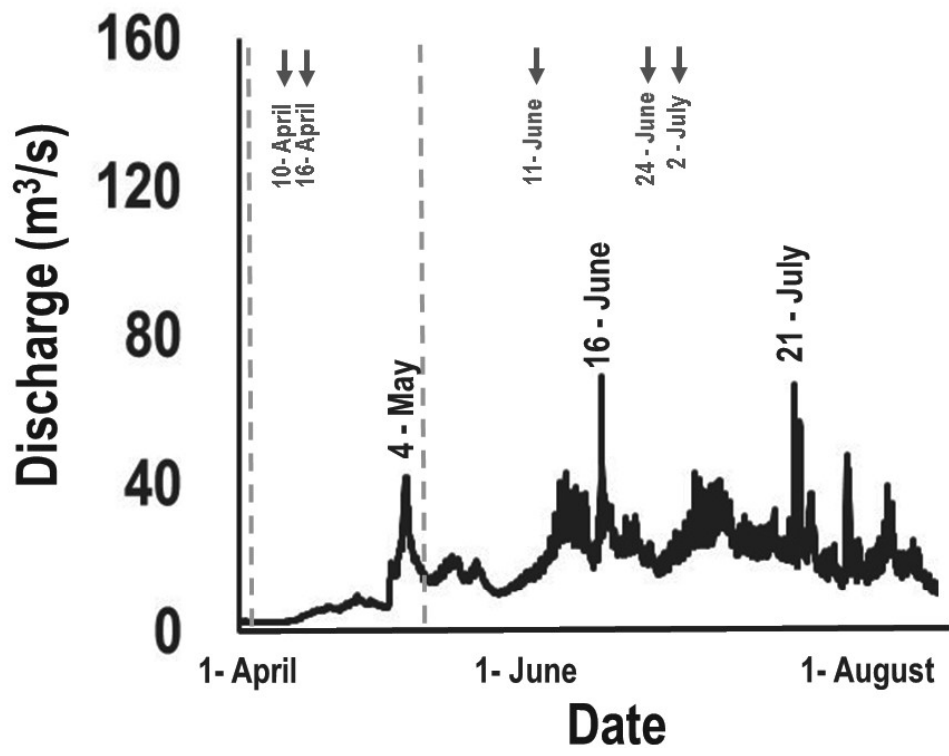


Figure 13



*Figure 14*

